

# Quantum transitions, ergodicity and quantum scars in coupled top model

Debabrata Mondal, Sudip Sinha, and S. Sinha

*Indian Institute of Science Education and Research-Kolkata, Mohanpur, Nadia-741246, India*

(Dated: March 16, 2022)

We consider an interacting collective spin model known as coupled top (CT), exhibiting a rich variety of phenomena related to quantum transitions and ergodicity, which we explore and find their connection with underlying dynamics. The ferromagnetic interaction between the spins leads to the quantum phase transition (QPT) as well as a dynamical transition at a critical coupling strength, and both the transitions are accompanied by excited state quantum phase transitions at critical energy densities. Above QPT, the onset of chaos in the CT model occurs in an intermediate coupling strength, which is analyzed both classically and quantum mechanically. However, a detailed analysis reveals the presence of non-ergodic multifractal eigenstates in the chaotic regime. We quantify the degree of ergodicity of the eigenstates from the relative entanglement entropy and multifractal dimensions, revealing its variation with energy density across the energy band. We probe such energy dependent ergodic behavior of states from non-equilibrium dynamics, which is also supplemented by phase space mixing in classical dynamics. Moreover, we identify another source of deviation from ergodicity due to the formation of ‘quantum scars’ arising from the unstable steady states and periodic orbits. Unlike the ergodic states, the scarred eigenstates violate Berry’s conjecture even in the chaotic regime, leading to the athermal non-ergodic behavior. Finally, we discuss the detection of non-ergodic behavior and dynamical signature of quantum scars by using ‘out-of-time-order correlator’, which has relevance in the recent experiments.

## I. INTRODUCTION

The study of the ground state, as well as excited states of interacting quantum systems, has become important for understanding various phenomena such as quantum phase transition (QPT), entanglement properties and more importantly, their ergodic behavior in non-equilibrium dynamics [1–5]. The QPT across a critical point leads to the ordering of the ground state, which is also reflected from the critical behavior of physical quantities at zero temperature [1]. In recent years, another type of quantum transition has been observed in collective models, where the excited states change their characteristics at a critical energy density corresponding to the singularities of density of states. Such transition is termed as excited state quantum phase transition (ESQPT) [6–12], however its connection with thermodynamic behavior of physical quantities deserves further attention [6, 11]. The non-equilibrium dynamics of a closed quantum system reveals various interesting phenomena related to ergodicity of the system, where the excited states also play a crucial role [4, 13]. In recent years, the ultracold atomic system has become a test bed to study the non-equilibrium properties of quantum many body systems [14, 15]. Certain many body systems after a quench evolve to a steady state corresponding to a generalized thermal distribution [16–21]. To understand thermalization of closed quantum systems, the eigenstate thermalization hypothesis (ETH) has been proposed, which attempts to explain ergodicity at the level of individual eigenstates [22, 23]. Moreover, its connection with random matrix theory (RMT) has been extensively explored in different quantum systems [3, 24, 25].

On the contrary, there are examples where thermaliza-

tion is absent, such as systems exhibiting many body localization (MBL) [26–28]. Apart from MBL, the presence of non-ergodic multifractal states [29–31] can also lead to the deviation from ergodicity and anomalous thermalization [32]. Tuning the parameters of quantum many body systems can change the nature of eigenstates, which in turn leads to the transition from MBL to ergodic or non-ergodic phases [33–39]. Recently, such non-ergodic and ergodic evolution has also been studied in quantum circuits [40, 41].

Beside the above mentioned cases, there are other sources of deviation from ergodicity, such as many body quantum scarring phenomena, which has recently been observed in an experiment on a chain of ultracold Rydberg atoms [42]. It has been found that a special choice of initial state exhibits periodic revival phenomenon and fails to thermalize, which has been attributed to many body quantum scar (MBQS) [43–47]. Such phenomena has also been analyzed theoretically in other interacting quantum models [48–59]. Originally, quantum scars in non interacting quantum system were identified as reminiscence of unstable classical orbits in a chaotic stadium [60]. However, such connection of unstable dynamics with MBQS in an interacting quantum system is not obvious and deserves further attention [46, 47, 58, 59].

Unlike the classical systems, the route to ergodicity and its deviation in closed quantum systems remains a challenging issue. In a classical system, the ergodicity due to phase space mixing arises from irregular behavior of chaotic trajectories, whereas such picture is unclear in a quantum system due to the absence of phase space trajectories. However, the connection between ergodicity and underlying chaotic dynamics of its classical counterpart has been explored in certain systems [61–63]. Moreover, the underlying chaos in a quantum sys-

tem can be detected by a newly developed tool known as ‘out-of-time-order correlator’ (OTOC), which allows us to investigate the route to ergodicity and its connection with underlying chaos [64–79]. In this context, it is also important to explore the connection between formation of MBQS in an interacting many body system and the underlying unstable dynamics, which has not been properly established. Such correspondence with classical description can elucidate the ergodic behavior of closed quantum systems and its deviation due to the formation of quantum scars, which is one of the main objectives of the present work.

In this work, we consider an interacting collective spin model known as coupled top (CT) model, exhibiting a variety of rich phenomena, which includes different type of quantum transitions, ergodic behavior and formation of quantum scars. We discuss the above mentioned phenomena in details and explore their connection with the underlying classical dynamics. The CT model undergoes a QPT at a critical coupling, above which the onset of chaos occurs in an intermediate range of coupling strength, where its ergodic behavior is investigated in details. Even in the chaotic regime, we identify the sources of deviation from ergodicity due to the presence of non-ergodic multifractal states and quantum scars, which can be detected from their dynamical signatures. Moreover, we elucidate the mechanism behind the formation of quantum scars arising from the unstable fixed points and periodic orbits. This work is an extension of our previous work [59], where we present an elaborate discussion and new results related to quantum transitions, ergodic properties and quantum scarring phenomena in the CT model.

The paper is organized as follows. In Sec.II, we describe the coupled top (CT) model and analyze it classically to obtain the steady states and their stability. Next, we study the various type of quantum transitions exhibited by this model and discuss their connection with the classical steady states in Sec.III. It undergoes a quantum phase transition (QPT) as well dynamical transition at a critical coupling, which is discussed in subsection III A, and the occurrence of excited state quantum phase transition (ESQPT) above the critical coupling is discussed in subsection III B. In Sec.IV, we investigate the onset of chaos both classically as well quantum mechanically, which are presented in subsections IV A and IV B respectively. Next, we investigate the ergodic properties of the eigenstates in Sec.V and discuss their multifractal behavior in subsection V A. Sec.VI contains a detailed discussion on quantum dynamics of CT model, and its classical quantum correspondence is explored in subsection VI A. The quantum dynamics of CT model is presented in Sec.VI, and its classical quantum correspondence is explored in subsection VI A. The manifestation of degree of ergodicity in non-equilibrium dynamics and its detection by using the ‘out-of-time-order correlators’ (OTOC), are discussed in subsections VI B and VI C respectively. The quantum scarring phenomena in CT model is inves-

tigated in Sec.VII, where we identify the two types of scars arising from unstable steady states and unstable periodic orbits, which are presented in subsection VII A and VII B. In subsection VII C, we discuss the detection of quantum scars from their dynamical signature using OTOC technique. Finally, we summarize the results and conclude in Sec.VIII. In appendix A, we outline the Holstein Primakoff approximation to obtain the excitation energies and spin fluctuations at QPT. In appendix B, we derive the effective potential corresponding to CT model, describing the QPT and ESQPT. The signature of QPT from multifractal dimensions is presented in appendix C. The integrability of CT model at an extreme coupling strength is discussed in appendix D.

## II. MODEL AND CLASSICAL ANALYSIS

The coupled top (CT) model [59, 80–84] describes the dynamics of two large spins of equal magnitude  $S$  interacting ferromagnetically with each other, analogous to transverse field Ising model [85]. This collective model is described by the following Hamiltonian,

$$\hat{\mathcal{H}} = -\hbar\omega_0 (\hat{S}_{1x} + \hat{S}_{2x}) - \frac{\mu}{S} \hat{S}_{1z} \hat{S}_{2z} \quad (1)$$

where  $\hat{S}_{ia}$  ( $a = x, y, z$ ) represent the spin operators corresponding to two spins ( $i = 1, 2$ ). The first term in Eq.(1) describes the precession of two non interacting spins around the  $x$ -axis with angular frequency  $\omega_0$ , while the second term denotes ferromagnetic interaction between them with coupling strength  $\mu$ . In rest of the paper, we scale energy (time) by  $\omega_0(1/\omega_0)$  and set  $\hbar = 1$ , unless otherwise mentioned.

The collective nature of the spins, in the limit  $S \rightarrow \infty$  allows us to study the model classically. In this limit, the  $\hat{s}_{ia} = \hat{S}_{ia}/S$  can be written in terms of the classical spin vector,

$$\vec{s}_i \equiv (s_{ix}, s_{iy}, s_{iz}) = (\sin \theta_i \cos \phi_i, \sin \theta_i \sin \phi_i, \cos \theta_i) \quad (2)$$

where  $\phi_i$  and  $\theta_i$  represent the orientation of the spins. Alternatively, the dynamics can be studied in phase space using the canonically conjugate variables  $\{\phi_i, z_i = \cos \theta_i\}$  and in terms of these collective variables  $\{z_1, \phi_1, z_2, \phi_2\}$ , the classical Hamiltonian can be rewritten as,

$$\mathcal{H}_{cl} = -\sqrt{1 - z_1^2} \cos \phi_1 - \sqrt{1 - z_2^2} \cos \phi_2 - \mu z_1 z_2 \quad (3)$$

where the Hamiltonian  $\mathcal{H}_{cl}$  and the classical energy  $E$  are scaled by spin magnitude  $S$ , therefore becoming an intensive quantity, independent of  $S$ . In general, we denote the collective variables as  $\mathbf{X} = \{z_1, \phi_1, z_2, \phi_2\}$  which represents the phase space point. The classical dynamics is described by the following equations of motion (EOM),

$$\dot{\phi}_i = \frac{z_i \cos \phi_i}{\sqrt{1 - z_i^2}} - \mu z_i \quad (4a)$$

$$\dot{z}_i = -\sqrt{1 - z_i^2} \sin \phi_i \quad (4b)$$

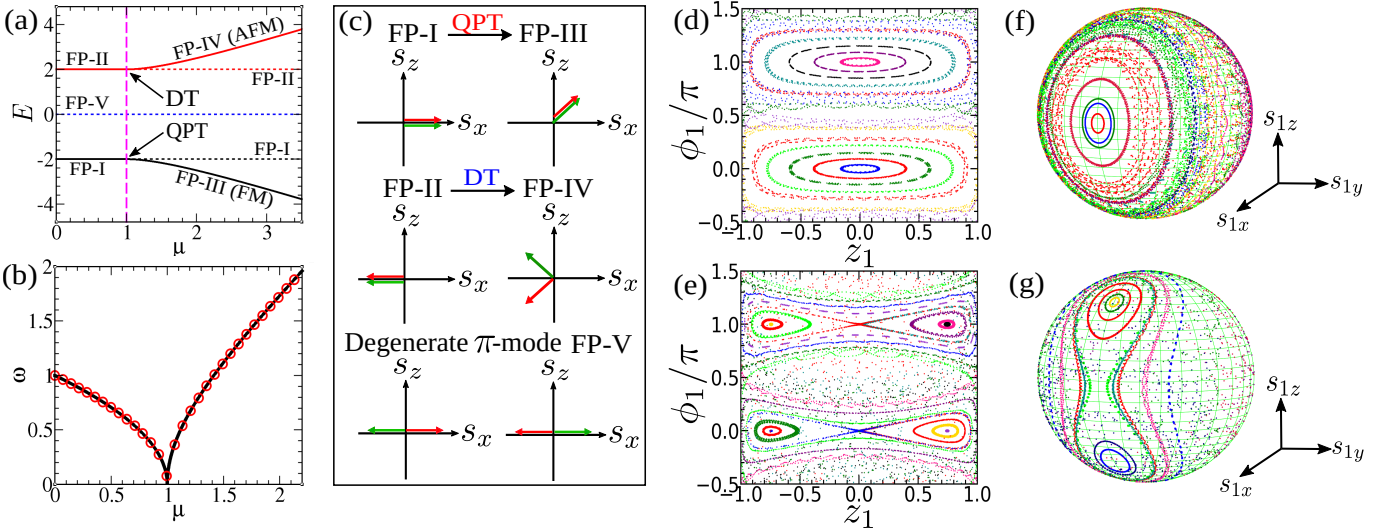


FIG. 1: (a) Various steady states with different energies as a function of  $\mu$ . Solid (dotted) lines represent stable (unstable) branches and vertical pink dashed line indicates the critical coupling  $\mu_c$ . (b) Small amplitude oscillation frequency  $\omega$  as a function  $\mu$  of the steady states corresponding to ground state (black solid line) and highest excited state (red circles), where vanishing of  $\omega$  at  $\mu_c = 1$  signifies QPT and dynamical transition. (c) Schematic diagram of spin configuration for different steady states. Phase portraits ((d) and (e)) and trajectories on Bloch sphere ((f) and (g)) exhibiting QPT and dynamical transition respectively. For (d),(f)  $\mu = 0.5 < \mu_c$  and (e),(g)  $\mu = 1.5 > \mu_c$ .

where  $\bar{i} \neq i$ . To capture the overall dynamical behavior, we first analyze the fixed points (FP) and their stability, varying the coupling strength  $\mu$ . The FPs describe the steady states which can be obtained by equating the LHS of Eq.(4) to zero and are denoted by  $\{z_1^*, \phi_1^*, z_2^*, \phi_2^*\}$ . To understand the stability of the steady states, we perform the linear stability analysis in the presence of small fluctuations around the FPs, which evolves as,  $\delta\mathbf{X}(t) = \delta\mathbf{X}(0)e^{i\omega t}$ . The frequency  $\omega$  of the small amplitude oscillation, is given by,

$$\omega_{\pm}^2 = \frac{1}{2} \left( A_1 + A_2 \pm \sqrt{(A_1 - A_2)^2 + 4\mu^2 \frac{\cos \phi_1^* \cos \phi_2^*}{\sqrt{A_1 A_2}}} \right) \quad (5)$$

where  $\omega_{\pm}$  are the frequencies of two collective modes and  $A_i = 1/(1 - z_i^{*2})$  for  $i = 1, 2$ . The stability of FPs is ensured if the oscillation frequencies  $\omega$  are real, equivalently  $\lambda_I = \text{Im}(\omega) = 0$ .

The steady states and their nature with increasing coupling strength are summarized in Fig.1(a), where we observe a characteristic change at a critical coupling strength  $\mu_c = 1$ . The nature of the FPs can be characterized by the Ising symmetry of the Hamiltonian, which remain invariant under  $s_{iz} \rightarrow -s_{iz}$ . For  $\mu < \mu_c$ , we find the following symmetry unbroken stable FPs, which are represented by,

$$(I) : z_1^* = 0, \phi_1^* = 0; z_2^* = 0, \phi_2^* = 0 \quad (6)$$

$$(II) : z_1^* = 0, \phi_1^* = \pi; z_2^* = 0, \phi_2^* = \pi \quad (7)$$

For FP-I (FP-II), both spins are aligned to positive (negative)  $x$ -axis, and have zero magnetization along  $z$ -axis, with energy  $E = \mp 2$ . Both FP-I and II become unstable

at  $\mu = \mu_c$  and undergo pitchfork bifurcation, giving rise to two pairs of stable symmetry broken steady states, which are given by,

$$(III) : z_1^* = z_2^* = \pm \sqrt{1 - 1/\mu^2}, \phi_1^* = \phi_2^* = 0 \quad (8)$$

$$(IV) : z_1^* = -z_2^* = \pm \sqrt{1 - 1/\mu^2}, \phi_1^* = \phi_2^* = \pi \quad (9)$$

where (FP-IV) FP-III represents (anti)ferromagnetic state with energy  $E = \pm(\mu + 1/\mu)$ , which corresponds to the maximum (minimum) energy of the classical Hamiltonian in Eq.(3). Both above and below the critical coupling  $\mu_c$ , the stable FPs corresponding to maximum and minimum energy states yield same frequencies of small amplitude oscillations, although their spin configurations are different. The oscillation frequencies for symmetry unbroken (FP-I, FP-II) and broken (FP-III, FP-IV) states are given by,

$$\omega_{\pm} = \begin{cases} \sqrt{1 \pm \mu} & \text{for } \mu < \mu_c \\ \sqrt{\mu^2 \pm 1} & \text{for } \mu \geq \mu_c \end{cases} \quad (10)$$

It is interesting to note that, the oscillation frequency  $\omega_-$  of the lower mode vanishes at  $\mu_c$  for both the bifurcations, as shown in Fig.1(b)).

In addition, there exists another degenerate pair of unstable FPs represented by (V)  $\{z_1^* = z_2^* = 0, \phi_1^* = \pi, \phi_2^* = 0\}$  and  $\{z_1^* = z_2^* = 0, \phi_1^* = 0, \phi_2^* = \pi\}$  with energy  $E = 0$ . We denote this as ‘ $\pi$ -mode’, since the relative angle between the spins is  $\pi$ . The instability exponent  $\lambda_I$  of the ‘ $\pi$ -mode’ (FP-V) is given by,

$$\lambda_I = \sqrt{\frac{(\mu^2 + 1)^{\frac{1}{2}} - 1}{2}} \quad (11)$$

which increases with the coupling strength  $\mu$ .

The schematic, explaining the spin configurations corresponding to the above FPs are given in Fig.1(c). To clearly visualize the fixed point structure and their bifurcation, we obtain the dynamics, by solving the EOM given in Eq.(4) and plot it over phase portrait in  $z_1 - \phi_1$  plane and Bloch sphere (see Fig.1(d-g)). It can be observed from Fig.1(d,f), for small coupling strength  $\mu < \mu_c$ , regular phase space trajectories are formed around the symmetry unbroken phases, whereas, above the critical point, the phase portrait contains regular trajectories around the symmetry broken FPs. However, the intermediate region of phase space is filled with irregular trajectories (see Fig.1(e)), indicating the onset of chaos, which is discussed in Sec.IV.

### III. QUANTUM TRANSITIONS IN COUPLED TOP MODEL

In this section, we discuss different types of quantum transitions exhibited by the CT model and identify their signature from the behavior of different physical quantities. The connection between these transitions with the fixed point structure and their bifurcation, obtained from classical analysis are also studied.

#### A. Quantum phase transition and Dynamical transition

As seen from the classical analysis, the bifurcation of the steady state FP-I to FP-III breaks the ising symmetry, which gives rise to a ferromagnetic ordering of spins in the ground state (GS). Such bifurcation of the minimum energy steady state is identified as quantum phase transition (QPT) leading to the ordering of GS. Similarly, the bifurcation of FP-II to FP-IV corresponds to a dynamical transition associated with the highest energy excited state, acquiring an antiferromagnetic ordering. Such type of dynamical transition has also been observed in Bose-Josephson junction [86, 87]. Quantum mechanically, both the QPT and dynamical transition can be identified from the changes in the relevant physical quantities computed for the GS and highest excited state respectively, which are obtained by diagonalizing the Hamiltonian given in Eq.(1). It is interesting to note that, both QPT and dynamical transition are related, since the transformation  $\hat{S}_x \rightarrow -\hat{S}_x$  and  $\mu \rightarrow -\mu$  changes the ground state of ferromagnetic coupled top to the excited state of the same model with antiferromagnetic interaction, which explains the antiferromagnetic ordering of the excited state after dynamical transition. Both QPT and dynamical transition can be captured by the characteristic changes in different physical quantities obtained for GS and excited state respectively, across  $\mu = \mu_c$  (see Fig.2). As a consequence of the symmetry between the GS and excited state, the complementary

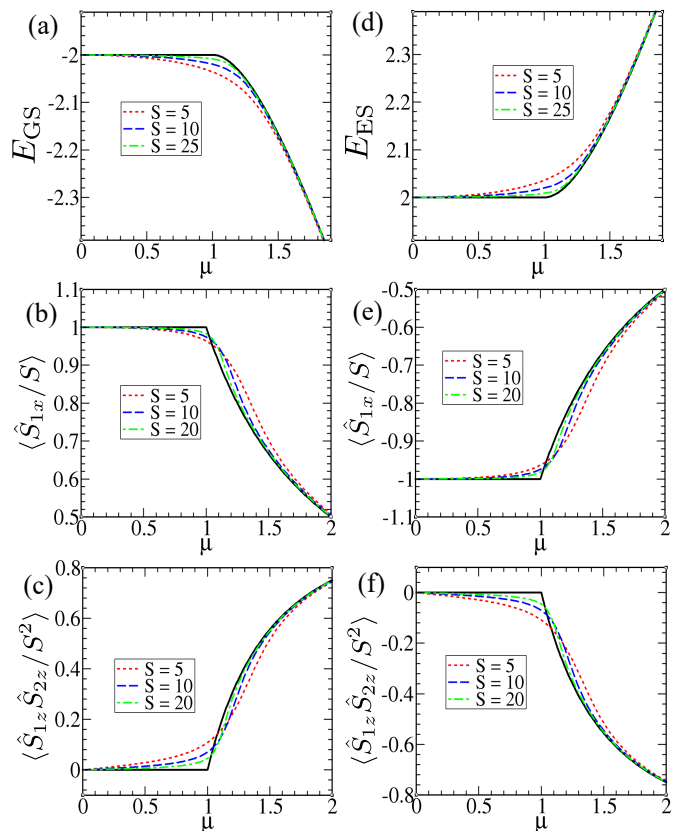


FIG. 2: Signature of QPT and dynamical transition: Variation of (a) ground state energy  $E_{GS}$ , (b)  $\langle \hat{S}_{1x} \rangle / S$ , (c)  $\langle \hat{S}_{1z} \hat{S}_{2z} \rangle / S^2$  as a function of coupling strength  $\mu$ . The second column (d,e,f) represents variation of same physical quantities as in (a,b,c) with  $\mu$ , corresponding to highest excited state, exhibiting dynamical transition. The black solid line in all the figures denote the classically obtained analytical result of the respective quantities.

behavior of the physical quantities (as shown in Fig.2) can be observed for QPT and dynamical transition, particularly, the expectation value of  $\hat{S}_{1z} \hat{S}_{2z} / S^2$ , captures the ferromagnetic and antiferromagnetic ordering due to the respective transitions (see Fig.2(c),(f)).

In the  $S \rightarrow \infty$  limit, the QPT can be analyzed within Holstein Primakoff (HP) approximation [88], which has been discussed in details in appendix A. The lowest excitation energy obtained from the HP method is in agreement with the small amplitude oscillation frequency (as shown in Fig.1(b)), which vanishes as  $\sim \sqrt{|\mu - \mu_c|}$ , signifying the mean field like behavior of QPT. As a consequence, the spin fluctuation diverges at the critical point, which can also be captured from the HP approximation. Moreover, within such semiclassical description, the spin system can equivalently be described in terms of the effective potential, which is discussed in appendix B. For  $\mu < \mu_c$ , the effective potential has a single minima corresponding to the symmetry unbroken phase, which changes its shape to a double well structure, clearly ex-

hibiting the symmetry breaking across the critical point.

Unlike the HP approximation (with  $S \rightarrow \infty$ ), for full quantum mechanical computation with finite size Hilbert space, the true phase transition with symmetry broken phase is absent. However, after the transition, the energy gap between the consecutive even-odd parity eigenstates (symmetry preserved) is suppressed exponentially with system size. Although, the finite size effect masks the sharp changes of the physical quantities at the critical point, however with increasing  $S$ , they approach the classically obtained analytical results, exhibiting such sharp features, as depicted in Fig.2. For comparison of the numerical results with the classical ones in Fig.2, we have appropriately scaled the different physical quantities and quantum mechanical energies  $\mathcal{E}_\nu$  by  $S$ , to make them intensive in nature. Note that, the classical energy is equivalent to quantum mechanical energy density ( $E \equiv \mathcal{E}_\nu/S$ ).

## B. Excited state quantum phase transition

Apart from QPT and dynamical transition, the CT model exhibits another kind of transition known as excited state quantum phase transition (ESQPT) [6–12], which describes the characteristic change in the nature of excited eigenstates across certain critical energy density. Both QPT and dynamical transition are accompanied by ESQPT, which occurs above critical coupling strength  $\mu_c$ , at a critical energy density  $E_c = \mp 2$ , corresponding to unstable symmetry unbroken steady states FP-I and II respectively. The essential feature of ESQPT is the singular behavior of density of states (DOS) at the critical energy density  $E_c$ . From the classical Hamiltonian  $\mathcal{H}_{cl}$  (Eq.(3)), DOS can be written as,

$$\rho(E) = \frac{\mathcal{C}}{4\pi^2} \int_{-1}^1 \int_{-1}^1 \int_0^{2\pi} \int_0^{2\pi} \delta(E - \mathcal{H}_{cl}) d\phi_1 d\phi_2 dz_1 dz_2 \quad (12)$$

Where  $\mathcal{C} = 1/4$  keeps the normalization condition  $\int \rho(E) dE = 1$ , which is useful for the comparison of the semiclassical result with the exact quantum mechanical DOS, obtained for a system with finite  $S$ . The DOS obtained from quantum mechanical energy spectrum, is in good agreement with the semiclassical result, as shown in Fig.3(a). For  $\mu > \mu_c$ , the derivative of the semiclassical DOS shown in the inset of Fig.3(a) reveals the singularities at the critical energy densities indicating ESQPT. Physically, above  $\mu_c$ , FP-I and II at critical energy densities  $E_c = \mp 2$  separate the symmetry unbroken states within the range  $-2 < E < 2$  from the symmetry broken states in the energy range  $E_{GS} < E < -2$  and  $2 < E < E_{ES}$  corresponding to QPT and dynamical transition respectively. The ESQPT corresponding to QPT can be elucidated in terms of the effective potential, as discussed in appendix B. Above the critical point, the effective potential takes a double well structure, where the energy of the barrier height at  $E = -2$  corresponds to the critical energy density  $E_c$  of the ESQPT, which clearly separates the ferromagnetically ordered symmetry broken states ( $E < E_c$ ) from the unbro-

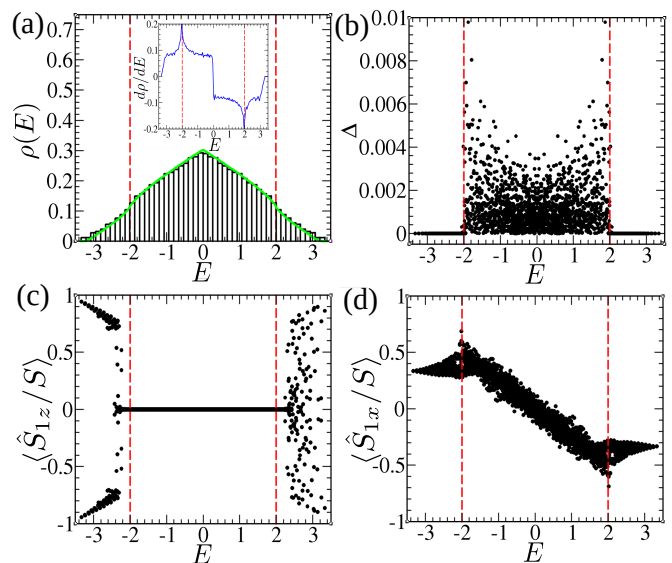


FIG. 3: Manifestation of ESQPT:(a) Density of states  $\rho(E)$  and its derivative  $d\rho/dE$  shown in the inset, (b) pair gap  $\Delta_\nu$ , (c)  $\langle \hat{S}_{1z}/S \rangle$  and (d)  $\langle \hat{S}_{1x}/S \rangle$  as a function of energy density  $E$  at  $\mu = 3$ . The red dashed lines marked at  $E = \pm 2$  indicate the critical energy densities corresponding to ESQPT. For quantum calculations, we choose  $S = 30$  in this and the rest of the figures, unless otherwise mentioned.

ken ones ( $E > E_c$ ). To understand the above mentioned behavior of the eigenstates, we compute the energy gap between consecutive even and odd parity states, defined as  $\Delta_\nu = \mathcal{E}_{2\nu} - \mathcal{E}_{2\nu-1}$ , which vanishes exponentially with increasing  $S$  for quasi degenerate states with  $|E| < |E_c|$  revealing their symmetry broken nature (see Fig.3(b)). Moreover, as shown in Fig.3(c,d), the expectation values of the observables like  $\langle \hat{S}_{1z}/S \rangle$  and  $\langle \hat{S}_{1x}/S \rangle$  clearly separate the symmetry unbroken states from symmetry broken sector with a significant change at  $E_c = \mp 2$  indicating ESQPT. The critical energy densities corresponding to ESQPT separating the symmetry broken and unbroken states, are also important for the ergodic nature of the eigenstates, which is discussed in the later part of this work.

## IV. ONSET OF CHAOS

In this section, we study the onset of chaos in the CT model, from the phase space dynamics and its reflection in the spectral statistics. In the weak coupling limit, the model exhibits an integrable structure, which represents two almost non interacting spins. The deviation from such regular dynamics occurs with increasing the coupling strength  $\mu$ , which is evident from the classical phase portrait shown in Fig.1(e,g). Above the critical coupling strength  $\mu_c$ , the regular region around the stable FPs shrinks and remaining part is filled up with chaotic trajectories, revealing a mixed phase space structure in

the intermediate regime of coupling. As  $\mu$  increases, the chaotic region in phase space continues to grow and it is eventually filled with irregular trajectories, at a fixed classical energy. This crossover from regular to chaotic regime can be captured from the Poincaré section corresponding to a fixed energy. However, it is important to note, in the extreme limit with  $\mu \gg 1$ , the integrability of the scaled Hamiltonian  $\hat{\mathcal{H}}/\mu$  can be recovered, which exhibits regular orbits around  $z$ -axis. Such integrable structure of the Hamiltonian and regular dynamics for  $\mu \gg 1$  is discussed in details in appendix D.

### A. Poincaré section and Lyapunov exponent

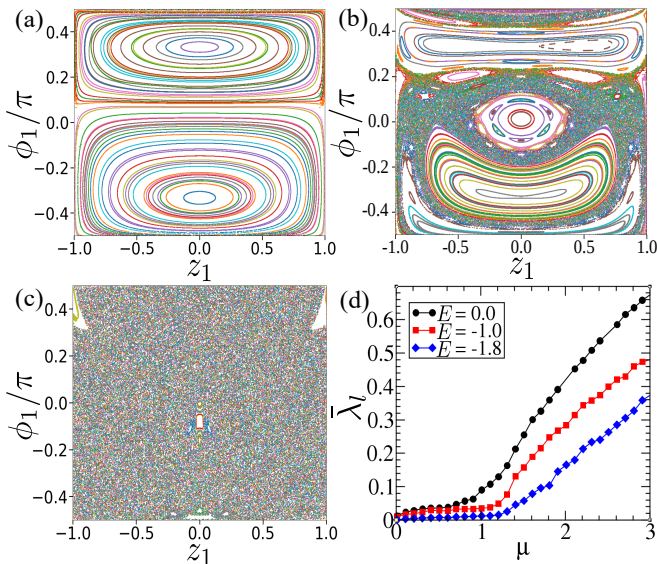


FIG. 4: Poincaré sections computed for  $z_2 = 0$  plane at a fixed energy  $E = -1.0$  for increasing coupling strength, (a)  $\mu = 0.5$ , (b)  $\mu = 1.2$ , (c)  $\mu = 1.85$ , depicting the onset of chaos. (d) Average Lyapunov exponent  $\bar{\lambda}_l$  with increasing  $\mu$  for different energies  $E$ , computed over an ensemble of 200 initial phase space points.

To capture the onset of chaos in the CT model, we study the Poincaré section [89] at the  $z_2 = 0$  plane for the dynamics with fixed energy  $E$ . As seen from Fig.4(a-c), for small coupling strength  $\mu < \mu_c$ , the Poincaré section contains only periodic orbits, signifying regular motion in phase space. Increasing  $\mu$  leads to the emergence of a number of chaotic trajectories that coexist with the periodic orbits, manifesting an interesting mixed phase space behavior. For large values of  $\mu$ , the phase space is completely filled up with chaotic trajectories, and the system becomes fully chaotic. In order to quantify the local chaotic behavior, we compute the Lyapunov exponent (LE)  $\lambda$  [89, 90], which is a standard measure to quantify the degree of chaos. Typically, for a chaotic trajectory, a small initial perturbation  $\delta\mathbf{X}(t = 0)$  at the phase space point  $\mathbf{X} = \{z_1, \phi_1, z_2, \phi_2\}$  grows exponentially in time

$\|\delta\mathbf{X}(t)\| = e^{\lambda t} \|\delta\mathbf{X}(0)\|$ , which yields the Lyapunov exponent,

$$\lambda = \lim_{t \rightarrow \infty} \frac{1}{t} \ln \left( \frac{\|\delta\mathbf{X}(t)\|}{\|\delta\mathbf{X}(0)\|} \right) \quad (13)$$

When the limit in Eq.(13) exists and  $\lambda$  is positive, the trajectories are sensitive to the initial condition and thus become chaotic in nature. The Lyapunov exponent  $\lambda$  can be computed by following the standard procedure described in [90, 91]. The overall chaotic behavior can be quantified by the average Lyapunov exponent  $\bar{\lambda}_l$ , which is obtained by averaging  $\lambda_l$ , computed for large sample of initial phase space points, corresponding to a fixed energy  $E$ . The growth of  $\bar{\lambda}_l$  above the critical coupling  $\mu_c$ , captures the onset of chaos, as depicted in Fig.4(d). Interestingly, the average LE  $\bar{\lambda}_l$  exhibits an energy dependence across the energy band, which increases towards the center of the band with  $E = 0$ .

### B. Spectral statistics

Although, it is not possible to quantify chaos from Lyapunov exponent quantum mechanically, due to the absence of phase space trajectories, however its signature can be captured from spectral statistics of the corresponding Hamiltonian. According to Berry Tabor's conjecture [92], the energy level spacing distribution of the system with regular dynamics follows Poisson statistics, whereas Bohigas-Giannoni-Schmit (BGS) conjecture[93] suggests, Wigner-Dyson distribution of level spacing for a classically chaotic system. To analyze the spectral statistics of the energy eigenvalues, we diagonalize the Hamiltonian given in Eq.(1) and obtain the eigenvalues  $\mathcal{E}_\nu$  corresponding to eigenvectors  $|\psi_\nu\rangle$ . Since the spectral statistics is performed for a particular symmetry sector, it is important to find out the symmetries of the CT model. The Hamiltonian in Eq.(1) remains invariant under the action of parity  $\hat{\Pi} = e^{i\pi(\hat{S}_{1x} + \hat{S}_{2x})}$  and spin exchange ( $S_1 \leftrightarrow S_2$ ) operator  $\hat{\mathcal{O}}$  [59], which flips the indices of basis states  $|m_{1z}, m_{2z}\rangle$ , where  $m_{iz}$  are the quantum numbers of  $\hat{S}_{iz}$ . Both the operators  $\hat{\Pi}, \hat{\mathcal{O}}$  possess two eigenvalues  $\pm 1$ , which we call as even (+1) and odd (-1). For spectral statistics, we consider the symmetry sector, for which both the eigenvalue of  $\hat{\Pi}$  and  $\hat{\mathcal{O}}$  are +1, without any loss of generality. Next, we arrange the eigenvalues corresponding to the said symmetry sector, in ascending order and compute the consecutive level spacings,  $\delta_\nu = \mathcal{E}_{\nu+1} - \mathcal{E}_\nu$ . Then, the normalized level spacing distribution is obtained by keeping the mean to be unity, following the standard procedure [94, 95]. As seen from Fig.5(a), the obtained level spacing distribution of energy eigenvalues agrees well with the Poisson statistics,  $P_P(\delta) = \exp(-\delta)$  for small coupling strength  $\mu < \mu_c$ , on the other hand, the spacing distribution exhibits level repulsion and approaches the Wigner-Dyson (WD) distribution,  $P_{WD}(\delta) = \frac{\pi}{2} \delta \exp(-\frac{\pi}{4} \delta^2)$  corresponding to

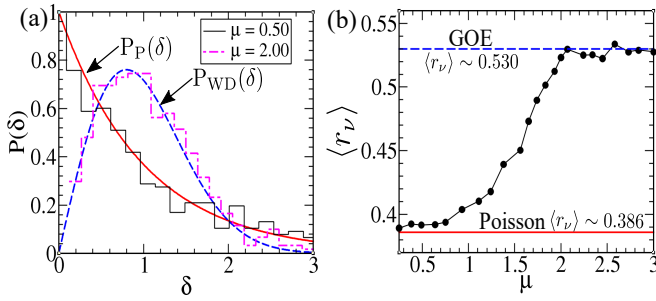


FIG. 5: (a) Level spacing distribution for regular ( $\mu = 0.50 < \mu_c$ ) and chaotic ( $\mu = 1.85 > \mu_c$ ) regime, which are compared with  $P_P(\delta)$  and  $P_{WD}(\delta)$  respectively. (b) Variation of average ratio of consecutive level spacing  $\langle r_\nu \rangle$  with increasing coupling strength  $\mu$ . Solid red (dashed blue) line indicates the value of  $\langle r_\nu \rangle$  corresponding to Poisson and GOE statistics respectively.

random matrix theory (RMT) of Gaussian orthogonal ensemble (GOE) for an intermediate range of coupling strength above  $\mu_c$ , where the underlying phase space becomes fully chaotic. The crossover from Poisson to Wigner-Dyson statistics of spacing distribution can also be captured from the average ratio of consecutive level spacing  $\langle r_\nu \rangle$  [96], which is given by ,

$$\langle r_\nu \rangle = \left\langle \frac{\min(\delta_\nu, \delta_{\nu+1})}{\max(\delta_\nu, \delta_{\nu+1})} \right\rangle \quad (14)$$

For Poisson matrix of level spacing,  $\langle r_\nu \rangle \approx 0.386$  [96], whereas in case of Gaussian orthogonal ensemble (GOE) of RMT,  $\langle r_\nu \rangle \approx 0.53$  [96]. Fig.5(b) shows the variation of  $\langle r_\nu \rangle$  with  $\mu$ , which clearly exhibits the crossover from Poisson to the WD statistics.

## V. ERGODIC BEHAVIOR AND MULTIFRACTALITY OF EIGENSTATES

In the previous section, we have investigated the onset of chaos in CT model at an intermediate coupling above the critical point, both classically and at the quantum level from the spectral statistics. In this section, we present a more detailed study of the eigenstates, which can reveal interesting phenomenon related to ergodicity and non-equilibrium dynamics. Since the entropy is related to the degree of chaoticity, we study entanglement entropy (EE) of the eigenstates  $|\psi_\nu\rangle$  of the Hamiltonian given in Eq.(1). To obtain the EE, we compute the reduced density matrix  $\hat{\rho}_S$  of a particular spin sector  $S$ , as follows,

$$\hat{\rho}_S = \text{Tr}_{\bar{S}} |\psi_\nu\rangle \langle \psi_\nu| \quad (15)$$

where  $\text{Tr}_{\bar{S}}$  denotes the partial trace with respect to the other spin sector. The EE quantifies the degree of entanglement, which is given by,

$$S_{en} = -\text{Tr} \hat{\rho}_S \log \hat{\rho}_S \quad (16)$$

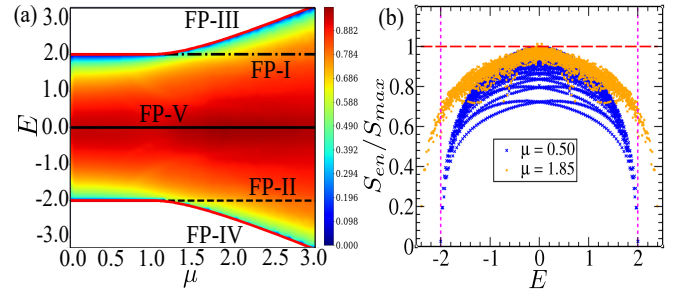


FIG. 6: Ergodic behavior of coupled top model: (a) Variation of relative entanglement entropy (EE)  $S_{en}/S_{max}$  (color plot) of eigenstates with energy densities  $E$  for increasing coupling strength  $\mu$ . (b) Variation of relative EE of eigenstates with energy density  $E$  for different coupling  $\mu$ . Horizontal red dashed line represents the maximum EE at unity. Pink dashed lines represent energy densities  $E_c$  corresponding to ESQPT.

We quantify the degree of ergodicity of a state by comparing the EE with its maximum value,

$$S_{max} \simeq \log(\mathcal{D}_A) - \mathcal{D}_A/2\mathcal{D}_B \quad (17)$$

which is obtained for a random state, partitioned into subsystems A(B) with dimensions  $\mathcal{D}_A(\mathcal{D}_B)$  [97]. Therefore, the relative EE  $S_{en}/S_{max}$  attains a maximum value at unity. In CT model we have  $\mathcal{D}_A = \mathcal{D}_B = 2S + 1$ , hence the maximum value of EE is given by  $S_{max} \simeq \log(2S + 1) - 1/2$ . From the comparison of the Lyapunov exponent obtained for the edge and center of the energy band ( shown in Fig.4(d)), we observe a variation in degree of chaoticity across the band, which is maximum at the band center, with classical energy  $E = 0$ . Interestingly, at the quantum level, the degree of ergodicity in terms of the relative EE  $S_{en}/S_{max}$  reveals the similar behavior with increasing energy density  $E$  across the energy band which is peaked at the center with energy density  $E = 0$  (see Fig.6(a)). Overall ergodic behavior of the CT model, in terms of the relative EE with increasing coupling  $\mu$ , across the QPT is shown as color scale plot in Fig.6(a). It is evident from Fig.6 that, after QPT, the symmetry broken eigenstates near the band edge are less ergodic compared to the symmetry unbroken states, which are separated by the ESQPT lines (FP-I,II). Above QPT, the relative EE of the eigenstates near band center with  $E \approx 0$  increases and attains its maximum value  $S_{en}/S_{max} \approx 1$  at an intermediate coupling strength  $\mu \approx 1.85$  (see Fig.6(b)), where the system becomes fully chaotic and  $\langle r_\nu \rangle$  approaches to GOE limit. As discussed earlier, since the model exhibits integrable behavior in the two extreme limits of coupling ( $\mu \ll 1$  and  $\mu \gg 1$ ), the system becomes maximally ergodic within a moderate range of coupling across  $\mu \approx 1.85$ , which is the main focus in the later part of this work.

### A. Multifractality of eigenstates

The localization and ergodic behavior of a state  $|\psi\rangle = \sum_{i=1}^{\mathcal{N}} \psi^i |i\rangle$  can be determined from the participation of the computational basis  $|i\rangle$  in the formation of said state. For a localized state, a few basis states participate with non vanishing  $\psi^i$ , whereas, for a fully ergodic state  $\psi^i \sim 1/\mathcal{N}$ , where  $\mathcal{N}$  is the dimension of the Hilbert space. In addition, the multifractal state lies in between these two extremes and their presence in a quantum many body system can give rise to an interesting non-ergodic behavior [98, 99]. Recently, it has been observed that the ground state of the quantum many body systems exhibit multifractality and the appearance of QPT in such systems can be captured from the change of multifractal dimensions [98, 100]. In appendix C, we also discuss how the QPT in CT model can be captured from the multifractal dimension of the ground state computed in a suitably chosen basis. The multifractal nature of the eigenstates  $|\psi_\nu\rangle$  can be captured from the statistical analysis of the coefficients  $\psi_\nu^i$  and their scaling with the dimensionality  $\mathcal{N}$ . To quantify the degree of localization of a state, the generalized inverse participation ratio (IPR) is given by,

$$I_q = \sum_i |\psi^i|^{2q} \quad (18)$$

which reduces to the usual IPR for  $q = 2$ . In general,  $I_q \sim 1/\mathcal{N}^{\tau_q}$  for sufficiently large dimension  $\mathcal{N}$ . In case of a localized state,  $\tau_q$  vanishes and  $I_q$  becomes independent of  $\mathcal{N}$ , whereas for an extended ergodic state,  $\tau_q \sim (q-1)$  as  $|\psi^i|^2 \sim 1/\mathcal{N}$ . Generally, the exponent can be written as  $\tau_q = (q-1)D_q$ , where  $D_q$  is the  $q$ th multifractal exponent characterizing the multifractality of the state. Alternatively,  $D_q$  can be calculated from the Rényi entropy  $S_R(q, \mathcal{N})$  as follows,

$$D_q = \lim_{\mathcal{N} \rightarrow \infty} \frac{S_R(q, \mathcal{N})}{\ln \mathcal{N}} \quad (19)$$

where the Rényi entropy is defined by,

$$S_R(q, \mathcal{N}) = -\frac{1}{(q-1)} \ln \left( \sum_i^{\mathcal{N}} |\psi^i|^{2q} \right). \quad (20)$$

For  $q \rightarrow 1$ , the Rényi entropy reduces to Shannon entropy  $S_{\text{Sh}} = -\sum_i^{\mathcal{N}} |\psi^i|^2 \ln |\psi^i|^2$  which yields the exponent  $D_1$ ,

$$D_1 = \lim_{\mathcal{N} \rightarrow \infty} \frac{S_{\text{Sh}}}{\ln \mathcal{N}}. \quad (21)$$

When the CT model becomes maximally chaotic ( $\mu \approx 1.85$ ), we investigate the multifractal properties of eigenstates with different energy densities using the above mentioned framework. For the eigenstates at the band center ( $E \approx 0$ ), the variation of generalized IPR  $I_q$  with dimension  $\mathcal{N}$  as shown in the log-log scale reveals the

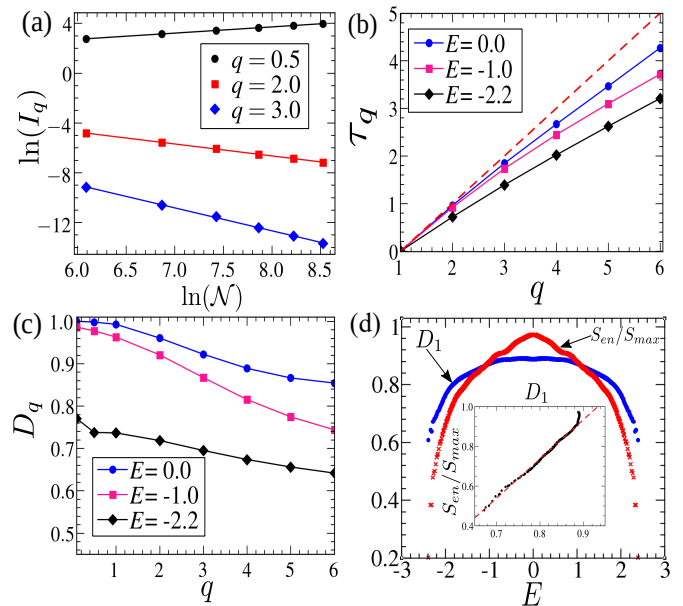


FIG. 7: Multifractality of the energy eigenstates: (a) Scaling of generalized IPR  $I_q$  with dimension  $\mathcal{N}$  for eigenstates at the band center with energy density  $E \approx 0$ . The solid lines represent the linear fit. (b) Variation of  $\tau_q$  with  $q$  for eigenstates with different values of  $E$ . The red dashed line represents  $\tau_q = q - 1$  with  $D_q = 1$ . (c) Multifractal dimension  $D_q$  (obtained from  $\tau_q$ ) as a function of  $q$  for different energy densities  $E$ . (d) Comparison between the multifractal dimension  $D_1$  and relative EE  $S_{en}/S_{max}$ , for eigenstates with increasing energy density  $E$  across the energy band. The linear behavior of  $D_1$  with  $S_{en}/S_{max}$  curve is shown in the inset of (d) and the red dashed line represents the corresponding linear fit. For all the figures,  $\mu = 1.85$ .

linear behavior (see Fig.7(a)) and the slope yields the exponent  $\tau_q$  for different  $q$ . As seen from Fig.7(b), the behavior of  $\tau_q$  with  $q$  deviates from linearity, indicating multifractal nature of the eigenstates. The multifractal dimension  $D_q$  can be extracted from  $\tau_q$ , and its variation with  $q$  for different energy densities is shown in Fig.7(c), which clearly exhibits the multifractal character of the eigenstates at different energy densities. The eigenstates at the band center with  $E \approx 0$  have multifractal dimension approaching to unity exhibiting the ergodic behavior of the states. However the deviation of  $D_q$  from unity for larger  $q$  values is expected due to the finite size effect, which is also present for eigenvectors of random matrices with finite dimensionality [101]. Away from the band center, the multifractal dimension  $D_q$  of the eigenstates decreases with increasing energy density  $|E|$ , indicating their non-ergodic nature. We plot the averaged multifractal dimension  $D_1$  with increasing energy density  $E$  across the energy band, which resembles with the behavior of relative EE, as depicted in Fig.7(d). Interestingly, the linear variation of relative EE  $S_{en}/S_{max}$  with multifractal exponent  $D_1$  (see inset of Fig.7(d)) has recently been observed for non-ergodic ‘sparse random

pure states' discussed in [102]. This behavior indicates that, both multifractal dimension  $D_1$  and relative EE  $S_{en}/S_{max}$  can quantify the degree of ergodicity, which is also reflected in the non-equilibrium dynamics, as discussed in [VIB](#).

## VI. QUANTUM DYNAMICS

In this section, we study the non-equilibrium dynamics of coupled top model to investigate the onset of chaos and related ergodic behavior. The time evolution of various observables can be studied from the time evolved state  $|\psi(t)\rangle = e^{-i\mathcal{H}t} |\psi(0)\rangle$  for a suitably chosen initial state  $|\psi(0)\rangle$ . To compare the quantum dynamics with its classical counterpart, we use the prescription of spin coherent state [103],

$$|z, \phi\rangle = \left(\frac{1+z}{2}\right)^S \exp\left\{\sqrt{\frac{1-z}{1+z}} e^{i\phi} \hat{S}_-\right\} |S, S\rangle \quad (22)$$

where  $z = \cos \theta$ , with  $\theta$  and  $\phi$  representing the orientation of the corresponding classical spin vector, providing a semiclassical description of a phase space point. The two spins of the CT model can be represented as the product of two corresponding coherent states,

$$|\psi_c\rangle = |z_1, \phi_1, z_2, \phi_2\rangle = |z_1, \phi_1\rangle \otimes |z_2, \phi_2\rangle \quad (23)$$

which provides a semiclassical description of phase space point. Such choice of an initial state as the spin coherent state allows us to probe the local ergodic behavior. Following this prescription, we next study the onset of chaos and the ergodic behavior from the non-equilibrium dynamics.

### A. Classical quantum correspondence

In this section, we compute the time evolution of the appropriately scaled physical observables obtained quantum mechanically and compare them with corresponding classical dynamics by solving the EOM, given in [Eq.\(4\)](#). For this purpose, we choose the initial coherent state representing the initial classical phase space point. For small coupling regime  $\mu \lesssim \mu_c$ , when the system exhibits regular dynamics, the time evolution of the expectation value  $\langle \hat{S}_{1z}/S \rangle$  is in good agreement with that of the classical dynamics [62], as shown in [Fig.8\(a\)](#). On the contrary, in the chaotic regime, the quantum evolution of the corresponding observable matches with its classical counterpart upto certain time scale, after which it deviates significantly with increasing time [62] (see [Fig.8\(b\)](#)). Moreover, the fluctuation corresponding to the above mentioned observable in the chaotic regime is much larger compared to the regular regime [62] and, systematic study of such fluctuations allows us to quantify chaos, which is discussed in the next subsection.

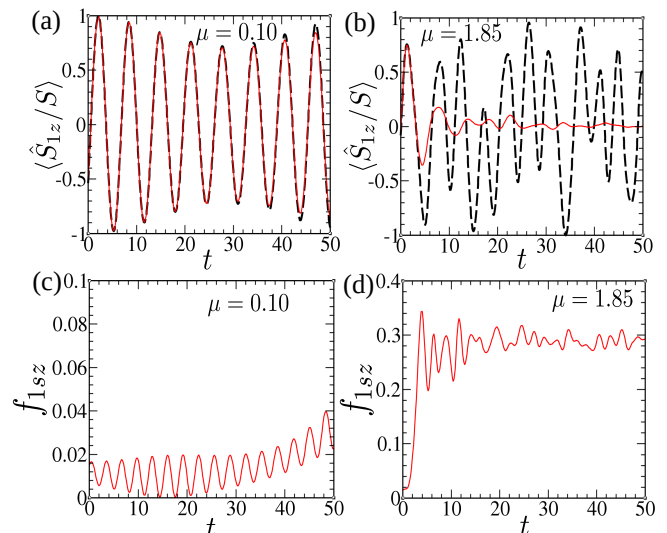


FIG. 8: Time evolution of the observable  $\langle \hat{S}_{1z}/S \rangle$  for (a)  $\mu = 0.1$  and (b)  $\mu = 1.85$ . The time evolution obtained from quantum dynamics (solid red line) is compared with the results obtained from classical dynamics using [Eq.\(4\)](#) (black dashed line). Time evolution of the spin fluctuation  $f_{1sz} = (\langle \hat{S}_{1z}^2 \rangle - \langle \hat{S}_{1z} \rangle^2)/S^2$  for (c)  $\mu = 0.1$  and (d)  $\mu = 1.85$ .

### B. Manifestation of ergodicity in non-equilibrium dynamics

To this end, we study the local ergodic behavior of CT model from the dynamics of different physical quantities. As seen from the analysis of the eigenstates in the previous section, the ergodic behavior of the eigenstates depends on their energy density  $E$ , even when the system becomes maximally chaotic.

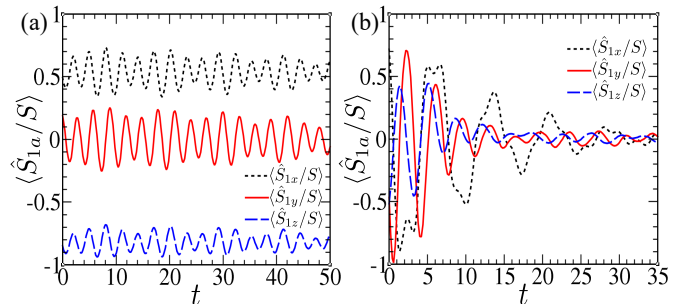


FIG. 9: Dynamics of different components of the spins ( $\langle \hat{S}_{1x,y,z}/S \rangle$ ) corresponding to the initial coherent state (a) near the band edge with  $E = -2.3$  and (b) at the band center for  $E = -0.01$ . For both the figures,  $\mu = 1.85$ .

We probe such behavior from non-equilibrium dynamics of the physical observables, starting from an initial coherent state with a given energy density  $E$ , since the energy remains conserved during the time evolution. In the maximally chaotic regime, we study the dynamics of the spin components  $\langle \hat{S}_{1a}/S \rangle$  ( $a = x, y, z$ ) by choos-

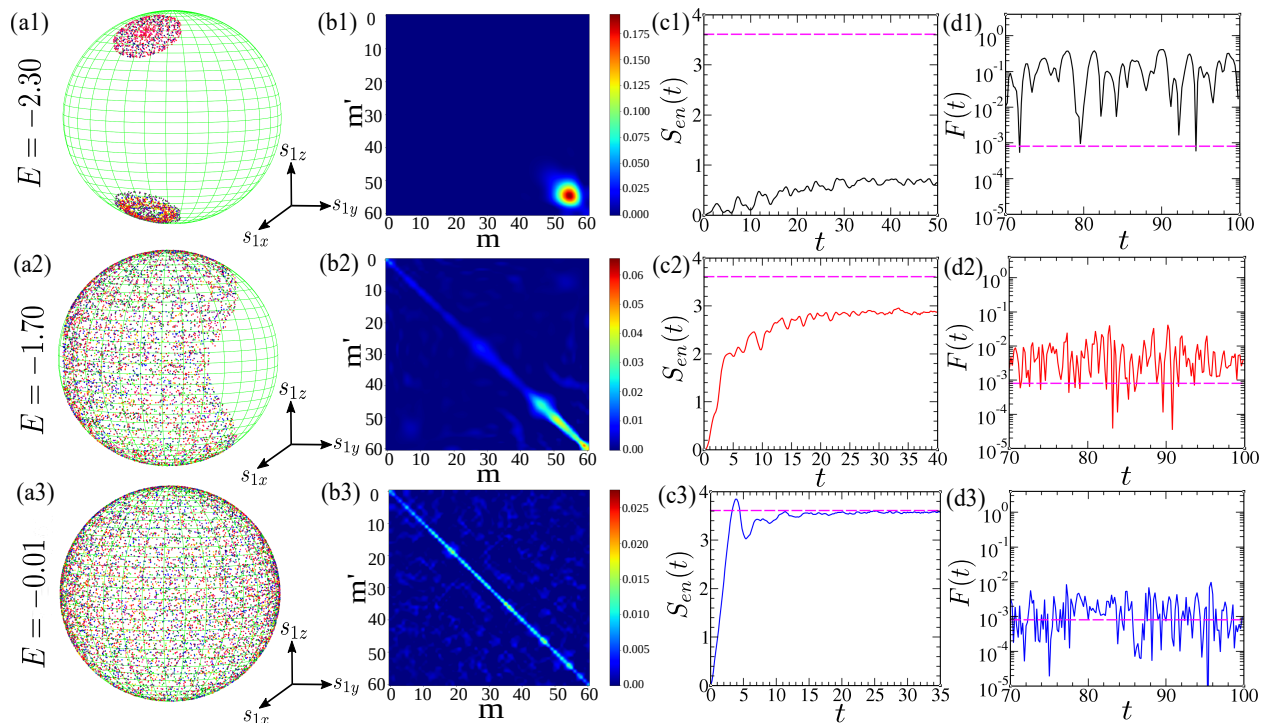


FIG. 10: Manifestation of degree of ergodicity in non-equilibrium dynamics of different physical quantities, with increasing energy density  $E$  (as shown in different rows). Column(a): The classical phase space trajectories on Bloch sphere with fixed classical energy  $E$ . Column(b): Color scale plot of the elements of final reduced density matrix  $(\hat{\rho}_S)_{mm'}$  (in the basis of  $\hat{S}_z$ ), after time evolution of an initial coherent state representing a phase space point corresponding to energy density  $E$ . Column(c) and (d) represent the time evolution of EE and survival probability respectively for the same initial coherent states. Horizontal pink dashed lines in column(c) and (d) denote maximum limit of EE (Eq.(17)) and GOE limit  $3/\mathcal{N}$  of survival probability respectively. Parameters chosen:  $\mu = 1.85$ .

ing two initial coherent states with energy density corresponding to the edge and center of the energy band. For dynamics with energy close to the band edge, the expectation values of the spin components exhibit oscillation without reaching any steady state, as shown in Fig.9(a). Moreover, the non vanishing value of  $\langle \hat{S}_{1z}/S \rangle$  reflects the symmetry broken nature of the states at the band edge. On the other hand, the dynamics with energy  $E \approx 0$  at the band center, evolves to a steady state with vanishing expectation value of all the spin components, exhibiting the ergodic behavior (see Fig.9(b)). This dynamical behavior supports the fact that the states near the center of the energy band almost reach the ergodic limit, whereas the states at the band edge deviate from it significantly, which is consistent with our previous analysis discussed in Sec.V.

To understand the dynamical signature of degree of ergodicity across the energy band in a more definitive manner, we study the evolution of EE [104–106] and the final reduced density matrix, as well the survival probability for different energy densities. For time evolution of  $|\psi(t)\rangle$  starting from an initial state  $|\psi(0)\rangle$ , the survival probability is defined as,

$$F(t) = |\langle \psi(t) | \psi(0) \rangle|^2 \quad (24)$$

Physically, it describes the memory of the initial state, which decays from unity and approaches to the GOE limit  $3/\mathcal{N}$  [25, 107] for ergodic evolution. At long time, the deviation of survival probability from the GOE limit can quantify the degree of ergodicity. Similarly, in the ergodic evolution, it is expected that the reduced density matrix  $(\hat{\rho}_S)_{mm'} = \langle m | \hat{\rho}_S | m' \rangle$  ( $|m\rangle, |m'\rangle$  are basis states of  $\hat{S}_z$ ) approaches to the microcanonical form with non vanishing diagonal elements giving rise to maximum EE  $S_{\max}$  given in Eq.(17). To gain more insight, we also study the corresponding phase space dynamics with fixed energy, projected on the Bloch sphere. The degree of ergodicity across the energy band from its edge to the center is summarized in Fig.10. For classical energy of ESQPT, the classical trajectories are confined within a small region around the symmetry broken fixed points (FP-III), clearly exhibiting a localized structure in Bloch sphere, as shown in Fig.10(a1). With increasing energy density  $E$ , the diffusive behavior of the trajectories is observed, which occupy the Bloch sphere partially, as shown in Fig.10(a2), and eventually cover the full Bloch sphere for  $E \approx 0$  (see Fig.10(a3)) corresponding to the center of energy band. Such behavior of increasing degree of ergodicity across the energy band is also reflected

from the final form of reduced density matrix, as well from the long time saturation of EE and survival probability, as depicted in respective columns of Fig.10(c,d). The degree of ergodicity of eigenstates across the energy band, as shown in Fig.6, is also reflected in the non-equilibrium dynamics. Moreover, the classical dynamics provides a connection between the phase space mixing and energy dependent ergodic behavior of its quantum counterpart. In the next subsection, we discuss a newly developed technique to probe the degree of ergodicity in a more systematic manner.

### C. OTOC dynamics

In recent studies, it has been shown that the dynamics of ‘out of time order correlator’ (OTOC) can be used as a tool to detect chaos in interacting quantum systems [64–79], which has also been implemented in NMR [71] and trapped ion experiments [72]. This was originally introduced in the context of superconductivity [108] and in recent years, it has also been applied in different areas of physics, most popularly in the context of black hole thermalization [64, 65], and scrambling of quantum information [70]. The growth rate of OTOC of appropriately chosen operators plays an analogous role of Lyapunov exponent for quantum systems [67, 74, 75]. Moreover, the recent studies reveal that its saturation value can also be used as a measure for degree of ergodicity [76–79]. The OTOC of two operators  $\hat{W}(t)$  and  $\hat{V}(0)$  is defined as follows,

$$O(t) = \text{Tr} \hat{\rho}_0 \hat{W}^\dagger(t) \hat{V}^\dagger(0) \hat{W}(t) \hat{V}(0) \quad (25)$$

where  $\hat{W}(t)$  represents the evolution of the operator at time  $t$  and  $\hat{\rho}_0$  is an appropriately chosen initial density matrix. This is related to the unequal time commutator  $C(t)$  defined as,

$$C(t) = \text{Tr} \hat{\rho}_0 [\hat{W}(t), \hat{V}(0)]^\dagger [\hat{W}(t), \hat{V}(0)] \quad (26)$$

which measures the non commutativity between these operators evolving with time, even if the operators commute initially. Both  $C(t)$  and  $O(t)$  are related by  $C(t) = 2(1 - \text{Re}O(t))$ , for unitary  $\hat{W}$  and  $\hat{V}$ . A generalization of OTOC known as the fidelity out of time order correlator (FOTOC) is defined for  $\hat{W} = e^{i\delta\phi\hat{G}}$  and  $\hat{V} = \hat{\rho}_0$ , for any hermitian operator  $\hat{G}$  and  $\hat{\rho}_0 = |\psi(0)\rangle\langle\psi(0)|$ , where  $|\psi(0)\rangle$  is the initial state. For a sufficiently small perturbation  $\delta\phi \ll 1$ , the FOTOC is related to the fluctuation  $f_G$  of the operator  $\hat{G}$  [74, 75],

$$1 - \mathcal{F}_G = \left( \langle \hat{G}^2 \rangle - \langle \hat{G} \rangle^2 \right) \delta\phi^2 \equiv f_G \delta\phi^2. \quad (27)$$

Therefore, measuring the fluctuations of appropriately chosen operators can quantify the degree of ergodicity. In the present work, we study the FOTOC corresponding

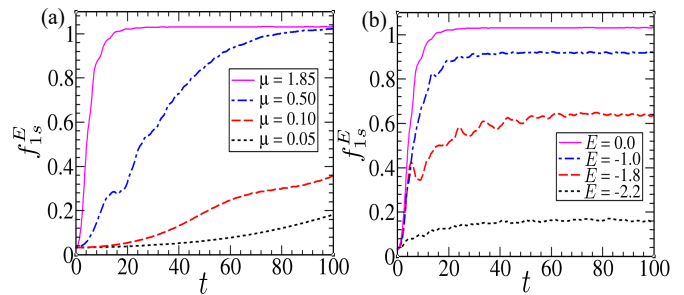


FIG. 11: Dynamics of average FOTOC  $f_{1s}^E$ , computed for an ensemble of initial coherent states with fixed energy density  $E$ . (a) Time evolution of  $f_{1s}^E$  for  $E \approx 0$ , corresponding to the band center, reflecting its change in degree of ergodicity with increasing coupling strength  $\mu$ . (b) Variation in dynamics of  $f_{1s}^E$  for different energy densities  $E$  across the energy band, reflecting the maximum degree of ergodicity at the band center for  $\mu = 1.85$ .

to the sum of fluctuations of all the spin components in a particular spin sector, which is given by,

$$f_{is} = \sum_{a=x,y,z} f_{isa} = \sum_{a=x,y,z} \left( \langle \hat{S}_{ia}^2 \rangle - \langle \hat{S}_{ia} \rangle^2 \right) / S^2. \quad (28)$$

In order to probe the ergodicity in an energy resolved manner, we define energy dependent FOTOC of spins  $f_{is}^E$ , which is obtained by averaging  $f_{is}$  over an ensemble of initial coherent states with a fixed energy density  $E$ . As depicted in Fig.11(a), the transition to chaos with increasing coupling strength  $\mu$  can be captured from the growth rate of  $f_{is}^E$  with  $E \approx 0$ . Moreover, in the chaotic regime, its saturation value approaches to unity, which is consistent with the fact that the states at the band center with  $E \approx 0$  become ergodic. Near the maximally chaotic region at  $\mu \approx 1.85$ , we investigate the energy dependent degree of ergodicity from the dynamics of  $f_{is}^E$  for different energy densities, which is shown in Fig.11(b). With increasing energy density  $E$ , corresponding to the energy band, from its edge to the centre, the growth rate of  $f_{is}^E$  as well as its saturation value increases which finally approaches to unity for  $E = 0$  (see Fig.11(b)). Such behavior, observed in FOTOC dynamics confirms the variation of degree of ergodicity across the energy band shown in Fig.6. The present analysis opens up the possibility for experimental investigation of local ergodic behavior of a quantum system using FOTOC technique, which has already been implemented in trapped ion system [74].

## VII. FORMATION OF QUANTUM SCARS

The investigation related to the fate of the unstable steady states in coupled top (CT) model reveals another source of deviation from ergodicity, due to the quantum scarring phenomena. In recent years, the study of quantum scars has regained interest due to the experimental observation of periodic revival and athermal behavior

of some special choice of initial state [42], which is attributed to many body quantum scar [43–47]. In the CT model, two types of scars are observed, which appear as reminiscence of unstable fixed points (FPs) and periodic orbits, as mentioned in our previous work [59]. In this section, we elaborate the discussion on above mentioned scars and present new results related to detection of dynamical signature of scars using FOTOC technique. In addition, we identify new scars and provide a systematic statistical analysis to identify the scarred eigenstates.

### A. Scars of unstable fixed points

To this end, we discuss about the quantum scars formed due to the unstable FPs. The reminiscence of the unstable FPs can be detected in some energy eigenstates in the form of a scar. Since such unstable FPs can be represented semiclassically in terms of the coherent states  $|\psi_c\rangle$ , the corresponding scarred eigenstates  $|\psi_\nu\rangle$  can be identified from the large overlap  $|\langle\psi_c|\psi_\nu\rangle|^2 \gg 1/\mathcal{N}$  [47, 58, 59], where  $\mathcal{N} = (2S + 1)^2$  is the dimension of the Hilbert space. In the ergodic regime, such overlap becomes  $O(1/\mathcal{N})$ , indicating delocalization. To visualize the scars, we compute the Husimi distribution obtained from the reduced density matrix  $\hat{\rho}_S$  of the corresponding scarred eigenstate  $|\psi_\nu\rangle$ ,

$$Q(z, \phi) = \frac{1}{\pi} \langle z, \phi | \hat{\rho}_S | z, \phi \rangle, \quad (29)$$

which provides a semiclassical phase space distribution. As seen from Fig.12(c,d), the Husimi distribution of the scarred eigenstates exhibits accumulation of phase space density near the corresponding unstable FPs, retaining their reminiscence at the quantum level.

In the present case, above the critical coupling  $\mu_c$ , the unstable ‘ $\pi$ -mode’ (FP-V), as well the two symmetry unbroken unstable steady states (FP-I, FP-II), as discussed in Sec.II, can manifest in the form of scars in the energy eigenstates. Since there are two degenerate spin configurations corresponding to the  $\pi$ -mode, to describe such state semiclassically, we consider the following linear combination of the coherent states,

$$|\pi_+\rangle = \frac{1}{\sqrt{2}} (|0, 0\rangle \otimes |0, \pi\rangle + |0, \pi\rangle \otimes |0, 0\rangle) \quad (30)$$

As shown in Fig.12(a), we identify the eigenstates bearing the scar of unstable  $\pi$ -mode from the maximum overlap with  $|\pi_+\rangle$ . The scarring of  $\pi$ -mode is evident from strong localization of Husimi distribution at  $\phi = 0$  and  $\pi$ , as depicted in Fig.12(b). Although the  $\pi$ -mode with energy  $E = 0$  coexists with the most ergodic states at the center of the energy band, the corresponding scarred eigenstates can be distinguished from their statistical properties. According to Berry’s conjecture [109], the eigenstates behave as random states in the ergodic regime and the probability distribution of their components  $\eta = |\psi_\nu^i|^2 \mathcal{N}$ , follows the well known Porter-Thomas

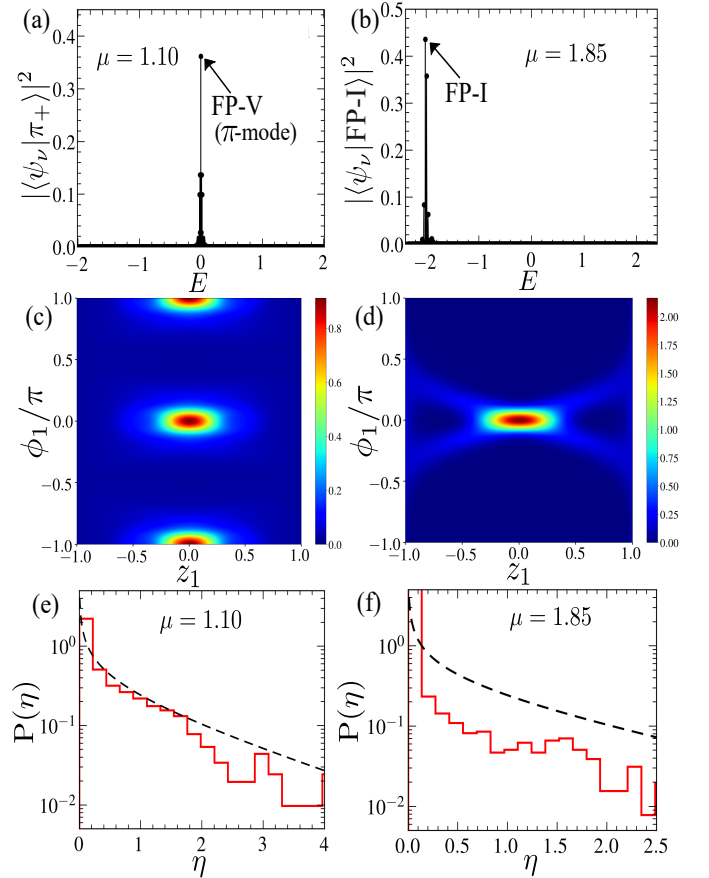


FIG. 12: Identification of eigenstates bearing the scars of unstable FPs. Overlap  $|\langle\psi_c|\psi_\nu\rangle|^2$  of eigenstates  $|\psi_\nu\rangle$  with coherent states  $|\psi_c\rangle$  corresponding to (a) the unstable  $\pi$ -mode and (b) FP-I. (c), (d) Husimi distribution for a particular spin sector of the eigenstate  $|\psi_\nu\rangle$  having maximum overlap (marked by arrowhead in (a), (b)). (e), (f) Distribution  $P(\eta)$  of the elements  $\eta = |\psi_\nu^i|^2 \mathcal{N}$  of the scarred eigenstates (marked by arrowhead in (a), (b)). The black dashed line represents the Porter-Thomas (PT) distribution.

(PT) distribution  $P(\eta) = (1/\sqrt{2\pi\eta}) \exp(-\eta/2)$  [94]. Interestingly, the eigenstates bearing scars deviate from PT distribution, indicating the violation of Berry’s conjecture [58, 59], as shown in Fig.12(e,f)). It is important to mention that, the magnitude of such deviation and the overlap with the corresponding coherent states, depend on the degree of scarring, which reduces with the enhanced instability of the underlying classical dynamics. A similar analysis reveals the scarred eigenstates corresponding to symmetry unbroken unstable steady state FP-I (see Fig.12(d-f)) at energy density  $E = -2$ . In a similar manner, the scar of equivalent symmetry unbroken steady state FP-II can also be identified at energy density  $E = +2$ . It is to be noted that, the degree of scarring of  $\pi$ -mode is much less compared to that of FP-I (or FP-II), as reflected from the deviation from PT distribution, shown in Fig.12(e,f), since the  $\pi$ -mode remains always unstable and the instability is much larger com-

pared to that of FP-I (or FP-II). Moreover, the steady state FP-I (or FP-II) is located away from the center of the energy band comprising of maximally ergodic states.

### B. Scars of periodic orbit and dynamical class

The second type of scars can be identified from the eigenstates maximally deviating from the ergodic limit at the center of the energy band with  $E \approx 0$ , where the majority of states approach to this limit. Such behavior can be revealed from the analysis of Shannon entropy  $S_{\text{Sh}} = -\sum_i |\psi_\nu^i|^2 \log |\psi_\nu^i|^2$  in a small energy window of  $\Delta E \sim 0.1$  around the band center  $E \approx 0$ , in the ergodic regime near  $\mu \approx 1.85$ . As seen from Fig.13(a), the Shannon entropy  $S_{\text{Sh}}$  for most of the states form a band like structure and approach the GOE limit  $\ln(0.48N)$  [24, 25], whereas there are a few states which have a lower value of  $S_{\text{Sh}}$  and deviate from it. Also, such states exhibit deviation from PT distribution (see Fig.13(f)). The Husimi distribution corresponding to these deviated states (as indicated by circles in Fig.13(a)) show a significant phase space localization, revealing the scars of periodic orbit, as depicted in Fig.13(c,d).

To understand the origin of such periodic orbits, we closely analyze the classical equations of motion (EOM) given in Eq.(4). As mentioned earlier, the CT model remains invariant under the exchange of two spins ( $S_1 \leftrightarrow S_2$ ). As a result, in terms of the redefined classical variables  $z_\pm = (z_1 \pm z_2)/2$  and  $\phi_\pm = (\phi_1 \pm \phi_2)/2$ , the overall dynamics of the system can be categorized into two classes, namely: **Class I** with  $\{z_+ = 0; \phi_+ = 0\}$ , and **Class II** for which  $\{z_- = 0; \phi_- = 0\}$  holds, where the dynamics is restricted on the reduced phase space of remaining variables. It can be verified from the equation of motion (EOM) in Eq.(4), either of the above conditions remain valid irrespective of the coupling strength  $\mu$  and the dynamics of the remaining variables reduces to that of the Lipkin-Meshkov-Glick (LMG) model [110] with (anti)ferromagnetic interaction corresponding to class (I)II. However, the presence of initial fluctuations violating such conditions corresponding to class I and II can lead to the instability of dynamics of the corresponding classes on the reduced phase space. By using the EOM in Eq.(4) and the conditions for both the classes, the dynamics of the remaining variables can be described by,

Class I:

$$\dot{z}_- = -\sqrt{1-z_-^2} \sin \phi_- \quad (31a)$$

$$\dot{\phi}_- = \frac{z_-}{\sqrt{1-z_-^2}} \cos \phi_- + \mu z_- \quad (31b)$$

Class II:

$$\dot{z}_+ = -\sqrt{1-z_+^2} \sin \phi_+ \quad (31c)$$

$$\dot{\phi}_+ = \frac{z_+}{\sqrt{1-z_+^2}} \cos \phi_+ - \mu z_+ \quad (31d)$$

where the dynamical class (I)II corresponds to the LMG

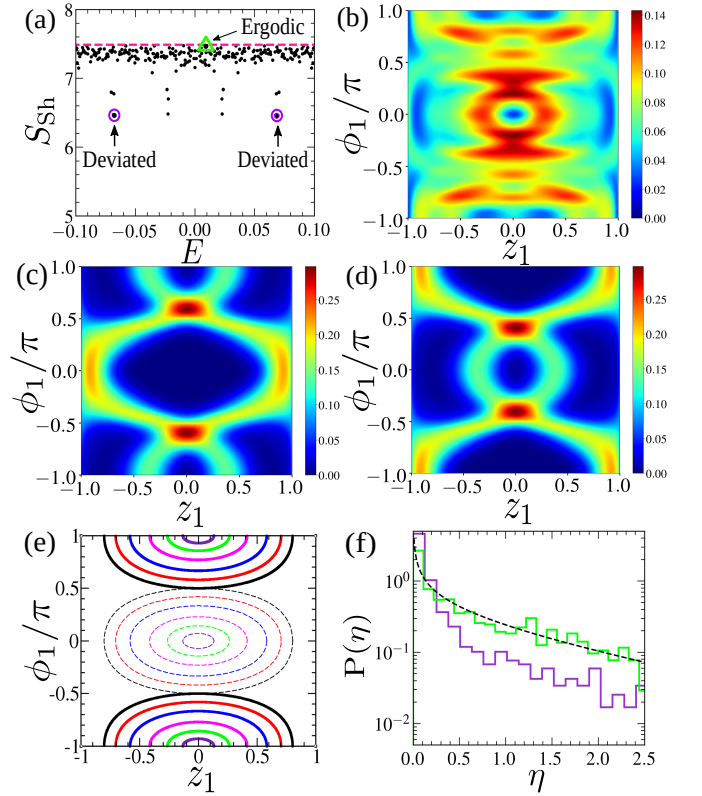


FIG. 13: Identification of eigenstates with scars of unstable periodic orbits: (a) Shannon entropy  $S_{\text{Sh}}$  of the eigenstates around the energy density  $E = 0$ . Husimi distribution for (b) an ergodic state marked by green triangle in (a), and for (c), (d) deviated states, marked by violet circles in (a), revealing the scar of periodic orbit. (e) Unstable orbits corresponding to class I (dashed lines) and II (solid lines). The outermost orbits of the two classes correspond to energy  $E = 0$ . (f) Comparison of distribution  $P(\eta)$  for the deviated scarred states (violet line) with that of an ergodic state (green line). The black dashed line corresponds to the PT distribution. For all figures,  $\mu = 1.85$ .

model with (anti)ferromagnetic interaction. From the above equations, we obtain the periodic orbits at energy  $E$  in a closed form, which can be written as,

$$z_\pm(t) = \mathcal{A} \text{cn} \left( \frac{\mathcal{A}\mu}{2k} (t + t_0), k \right) \quad (32a)$$

$$\cos(\phi_\pm(t)) = -\frac{E + \xi\mu z_\pm^2(t)}{2\sqrt{1-z_\pm^2(t)}} \quad (32b)$$

where cn is the Jacobi elliptic function with elliptic modulus  $k < 1$  and the constants are given by,

$$\mathcal{A}^2 = \frac{2}{\mu^2} \left[ -\xi \frac{\mu E}{2} - 1 + \Omega \right], \quad k^2 = \frac{1}{2} \left[ 1 - \frac{\xi E \mu / 2 + 1}{\Omega} \right],$$

$$t_0 = \frac{\text{F}(\cos^{-1}(z_\pm(0)/\mathcal{A}), k)}{\Omega^{1/2}}, \quad \Omega = \sqrt{\mu^2 + 1 + \xi E \mu}$$

The periodic orbits corresponding to dynamical class (I)II have energy in the range  $-2 < E < 0$  ( $0 <$

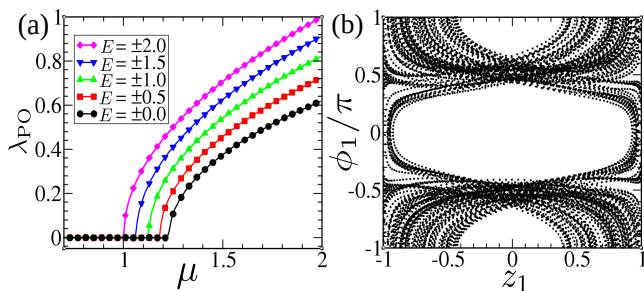


FIG. 14: Instability of periodic orbits belonging to the dynamical class (I or II). (a) Lyapunov exponent  $\lambda_{PO}$  for the periodic orbits (with energy  $E$ ) associated with the dynamical classes, as a function of coupling  $\mu$ . (b) Time evolution of a periodic orbit corresponding to dynamical class II with energy  $E \approx 0$ , in presence of a small constrain violating initial perturbation  $z_-(0) = \delta z \ll 1$ , in the unstable region with  $\mu = 1.4$ .

$E < 2$ ) and the parameter value  $\xi = -1(+1)$ , which determines the sign of the effective LMG model with (anti)ferromagnetic interaction (as seen from Eq.(31b) and Eq.(31d)). Such orbits with different energies belonging to the dynamical classes I and II are shown in Fig.13(e). The periodic orbits corresponding to the classes I and II are formed around the unstable steady states FP-I and FP-II respectively, and the orbits with equal and opposite energies have identical shapes, however their centres are shifted around the corresponding FPs (see Fig.13(e)). Interestingly, the largest orbits with energy  $E = 0$  belonging to the two different dynamical classes touch at  $\{z_1 = 0, \phi_1 = \pm\pi/2\}$ , where the accumulation of phase space density is exhibited in the Husimi distribution of the corresponding scarred eigenstates, as shown in Fig.13(c,d). The time period of such orbits with energy  $E = 0$  is given by,

$$T = \frac{4K(k)}{(1 + \mu^2)^{1/4}} \quad (33)$$

where  $K(k) = F(\pi/2, k)$  is the complete elliptic integral of first kind and  $F(\phi, k) = \int_0^\phi dx (1 - k^2 \sin^2 x)^{-1/2}$  [111]. Next, we investigate the stability of such periodic orbits by using the method of Monodromy matrix described in [90, 91]. Similar to the stability analysis of a phase space trajectory described in Sec.IV A, we calculate the Lyapunov exponent  $\lambda_{PO}$  starting from a point on the periodic orbit over its time period  $T$  and the instability of the corresponding orbit can be quantified from  $\lambda_{PO} > 0$ . The variation of Lyapunov exponent  $\lambda_{PO}$  with increasing coupling strength  $\mu$  is shown in Fig.14(a) for periodic orbits with different classical energies  $E$ . As seen from this figure, the largest periodic orbits with  $E = 0$  become unstable for  $\mu > \mu_u = 1.23$ , which ensures that these orbits in the ergodic regime ( $\mu \approx 1.85$ ) are indeed unstable. However, the reminiscence of such unstable orbits are still visible in the form of scars, which is evident from the Husimi distribution of the corresponding eigenstates,

as shown in Fig.13(c,d). It is evident from Fig.14(a), the smaller periodic orbits with increasing  $|E|$  (from  $E = 0$ ) become successively unstable for  $\mu < \mu_u$ , which finally terminates at  $\mu_c = 1$  for  $E = \pm 2$  corresponding to the unstable steady states FP-I and FP-II, around which such periodic orbits are formed. Moreover, we observe that the  $\lambda_{PO}$  for  $E = \pm 2$  coincides with the imaginary part of the small amplitude oscillation frequency  $\text{Im}(\omega) = \sqrt{\mu - 1}$ , corresponding to FP-I and FP-II, as discussed previously in Sec.II. From the full phase space dynamics, we identify that, the instability of such periodic orbits belonging to a particular dynamical class stems from the initial perturbations violating the constraints of the corresponding class. In Fig.14(b), we elucidate such dynamics in presence of small initial perturbation deviating from a particular dynamical class, which clearly leads to instability of the periodic orbits, however, the irregular trajectory remains localized around the corresponding orbits of both the dynamical classes, resembling the shape of the scar, as observed from the Husimi distributions in Fig.13(c).

### C. Dynamical signature of scars

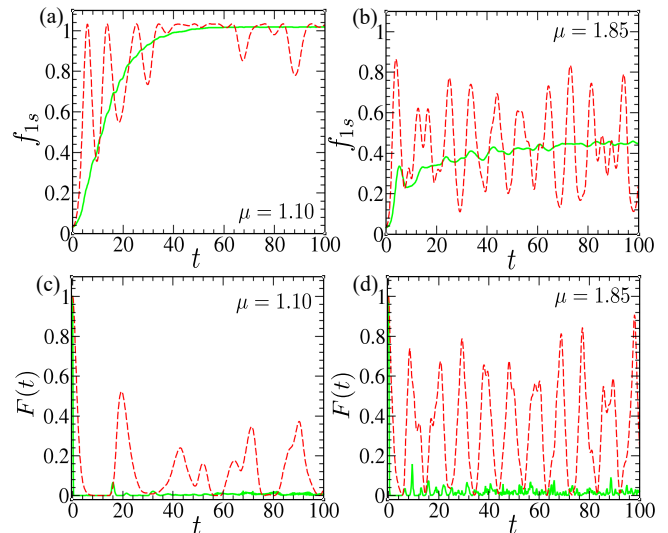


FIG. 15: Dynamical signature of quantum scars: Dynamics of FOTOC  $f_{1s}$  starting from the initial coherent state  $|\psi_c\rangle$ , representing the unstable FP of (a)  $\pi$ -mode and (b) FP-I, which is compared with average FOTOC  $f_{1s}^E$  (green line) corresponding to same energy density  $E$  of the respective unstable FPs. Survival probability  $|\langle\psi(t)|\psi_c\rangle|^2$  corresponding to unstable (c)  $\pi$ -mode and (d) FP-I. Green line corresponds to survival probability starting from an initial coherent state representing an arbitrary phase space point with same energy  $E$  of the above mentioned FPs.

To this end, we discuss the detection of two types of scars from their dynamical signature using the method of out-of-time order correlators (OTOC) and survival probability. In Sec.VIC, we outline the OTOC technique and

its extension Fidelity OTOC (FOTOC) which has been used to probe the local ergodic behavior of phase space. Since the first type of scars arise from the unstable FPs such as FP-V,I and II, it is more convenient to detect their signature from FOTOC dynamics. Given that, the FOTOC is directly related to the fluctuation of the corresponding operator, here we investigate the behavior of total spin fluctuation  $f_{1s}$ , defined in Eq.(28) to probe the presence of first type of scar. Starting from an initial coherent state representing the unstable FPs, the dynamics of the total spin fluctuations  $f_{1s}$  exhibits oscillations with large magnitude, as depicted in Fig.15(a,b). For comparison, we also compute the mean value of FOTOC  $f_{1s}^E$  (discussed in Sec.VIC) averaged over an ensemble of initial coherent states with energy density  $E$  corresponding to that of the unstable FP. As observed from Fig.15(a,b), the  $f_{1s}^E$  exhibits a smooth behavior and saturation in absence of oscillations, in contrast to the oscillatory behavior of  $f_{1s}$  for unstable FPs. We also observed that the oscillations in the dynamics of  $f_{1s}$  decrease as the overlap of the initial coherent state with that corresponding to the unstable FP reduces. Since the quantum scars lead to the deviation from ergodicity and retain the memory of the initial states, they can also be detected from the survival probability  $F(t) = |\langle \psi(t) | \psi(0) \rangle|^2$ , describing the overlap of time evolved state  $|\psi(t)\rangle$  with the initial state  $|\psi(0)\rangle$ . The time evolution of survival probability starting from the initial coherent state representing the FP-V and FP-I are shown in Fig.15(c,d). The revival phenomena as observed in the survival probability, for the initial coherent states corresponding to the unstable steady states, is a characteristic of such scarred states [43], which is absent in the ergodic evolution. Also, the survival probability at long time differs from the GOE limit, indicating the deviation from ergodicity.

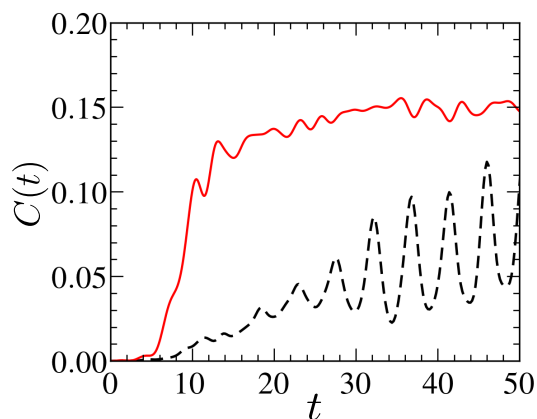


FIG. 16: Signature of scar of unstable periodic orbit obtained from OTOC dynamics. Time evolution of  $C(t)$  corresponding to two different initial density matrix,  $\hat{\rho}_0$  (black dashed line) and  $\hat{\rho}_{mc}$  (red solid line), as described in the main text, for  $\mu = 1.85$ . Dynamics of OTOC corresponding to scarred states (black dashed line) exhibits oscillation with periodicity close to time period  $T$  (see Eq.(33)) of the unstable periodic orbit.

We detect the dynamical signature of second type of scars corresponding to the unstable periodic orbits using the unequal time commutator of spins,  $C(t) = -\text{Tr} \hat{\rho}_0 [\hat{S}_z(t)/S, \hat{S}_z(0)/S]^2$ , which is also discussed in Sec.VIC. Next, we study the time evolution of  $C(t)$  for initial density matrix  $\hat{\rho}_0 = |\psi(0)\rangle \langle \psi(0)|$  constructed from the eigenstates carrying such scars, which are located near the band center, where the majority of states are ergodic (see Fig.13(a)). For comparison, we also investigate  $C(t)$  evaluated for initial microcanonical density matrix  $\hat{\rho}_{mc} = \sum_j |\psi_j\rangle \langle \psi_j| / \mathcal{N}_\Delta$  constructed from  $\mathcal{N}_\Delta$  ergodic states within a small range of energy density  $\Delta E$  at the center of the band. As seen from Fig.16, the unequal time commutator  $C(t)$  corresponding to the scarred eigenstate exhibits oscillatory behavior, in contrast to the  $C(t)$  showing a rapid growth and saturation in absence of oscillations for the ergodic states. The oscillatory behavior observed in FOTOC, as well in the unequal time commutator can be considered as a detectable signature for both types of scars.

## VIII. CONCLUSION

To summarize, we have investigated various aspects of the coupled top (CT) model related to different types of quantum transitions and ergodic behavior, revealing their connection with the underlying classical dynamics. The collective nature of the CT model with large magnitude of spins allows us to analyze the system classically, which elucidates the dynamical route to ergodicity and its deviation due to the formation of quantum scars. Ferromagnetic interaction between the spins lead to the quantum phase transition (QPT), as well as dynamical transition at a critical coupling strength  $\mu_c = 1$ , which gives rise to ferromagnetic and anti-ferromagnetic ordering of the ground state and highest excited state respectively. Above  $\mu_c$ , both QPT and dynamical transition are accompanied by two excited state quantum phase transitions (ESQPT) with critical energy densities corresponding to the symmetry unbroken unstable steady states. Such critical energy density corresponding to two ESQPT, separates the symmetry unbroken eigenstates at the central of the energy band from the symmetry broken states at the band edges. Interestingly, in two extreme limits of coupling strengths,  $\mu \ll 1$  as well for  $\mu \gg 1$ , the CT model exhibits integrability with regular dynamical behavior, and a crossover to chaos occurs in an intermediate range of coupling above  $\mu_c$ . At the quantum level, the overall chaotic behavior is detected from the spectral statistics, however a closer investigation reveals the existence of non-ergodic multifractal eigenstates across the energy band. We quantify the degree of ergodicity of eigenstates from relative entanglement entropy and multifractal dimensions, both of which resembles similar shape with increasing energy density across the energy band. In the maximally chaotic regime, only the eigenstates near the centre of the energy band approach er-

godic limit, whereas the degree of ergodicity of states decreases toward the band edge. We have shown, how such ergodic behavior of the energy band can be probed from non-equilibrium dynamics, which is also supplemented by corresponding phase space dynamics, elucidating the connection between phase space mixing and ergodicity of its quantum counterpart. More importantly, present analysis reveals another source of deviation from ergodicity due to the formation of two types of quantum scars, which arises as a reminiscence of unstable fixed points and periodic orbits. We present systematic methods to identify such eigenstates bearing quantum scars, which are found to be violating Berry's conjecture in contrast to the ergodic states. Finally, we have shown how degree of ergodicity and dynamical signature of quantum scars can be detected by using a newly developed technique known as out-of-time-order correlator, which has already been implemented in cold ion experiments [71, 72].

In conclusion, present work demonstrates a rich variety of phenomena observed in a simple collective spin model known as coupled top model, which also elucidates dynamical route to ergodicity of its quantum counterpart and quantum scarring phenomena in presence of interaction. The present analysis sheds light on the route to formation of quantum scars and their detection, that can be relevant in the context of newly observed many body quantum scars.

### Appendix A: Holstein Primakoff transformation

For large magnitude of spins  $S \gg 1$ , the coupled top (CT) model can be analyzed semiclassically by using Holstein Primakoff (HP) approximation [88], where  $1/S$  is considered to be a small parameter. When the classical spin vector is aligned along the  $z$ -axis, the corresponding spin operators in HP transformations can be written as,

$$\tilde{S}_{iz} = S - \hat{a}_i^\dagger \hat{a}_i \quad (\text{A1a})$$

$$\tilde{S}_{i+} = \sqrt{2S - \hat{a}_i^\dagger \hat{a}_i} \hat{a}_i \quad (\text{A1b})$$

$$\tilde{S}_{i-} = \hat{a}_i^\dagger \sqrt{2S - \hat{a}_i^\dagger \hat{a}_i} \quad (\text{A1c})$$

where the index  $i = 1, 2$  represents two spins of CT model and  $\hat{a}_i$  is bosonic annihilation operator describing the quantum fluctuations around the classical spin. As discussed in Sec. II, corresponding to the classical spin configuration of the ground state, both the spins of CT model lie in the  $x - z$  plane making an angle  $\theta_i$  with the  $z$ -axis which depends on the coupling  $\mu$ . For such orientation of the classical spin vectors, corresponding spin operators in HP representation can be obtained by performing a rotation about the  $y$ -axis,

$$\hat{S}_{ix} = \tilde{S}_{ix} \cos \theta_i + \tilde{S}_{iz} \sin \theta_i \quad (\text{A2a})$$

$$\hat{S}_{iz} = \tilde{S}_{iz} \cos \theta_i - \tilde{S}_{ix} \sin \theta_i \quad (\text{A2b})$$

Using these spin operators, the Hamiltonian given in Eq.(1) can be written in a series of  $1/S$ ,

$$\hat{\mathcal{H}} = S\mathcal{H}_0 + \sqrt{S}\hat{\mathcal{H}}_1 + \hat{\mathcal{H}}_2 + O(1/\sqrt{S}) \quad (\text{A3})$$

where the dominant term  $\mathcal{H}_0$  represents the classical energy density. Minimizing the classical energy  $\mathcal{H}_0$ , we obtain the following conditions,

$$\cos \theta_i = \begin{cases} 0 & \text{for } \mu < 1 \\ \pm \sqrt{1 - 1/\mu^2} & \text{for } \mu \geq 1 \end{cases} \quad (\text{A4})$$

which represents the spin orientation of the ground state. Next term in the Hamiltonian  $\hat{\mathcal{H}}_1$  vanishes for such ground state spin configuration. Finally, the Hamiltonian  $\hat{\mathcal{H}}_2$  describing the quantum fluctuations can be written as,

$$\hat{\mathcal{H}}_2 = \epsilon \hat{a}_1^\dagger \hat{a}_1 + \epsilon \hat{a}_2^\dagger \hat{a}_2 - \frac{\Gamma}{2} (\hat{a}_1 + \hat{a}_1^\dagger)(\hat{a}_2 + \hat{a}_2^\dagger) \quad (\text{A5})$$

where the parameters are given by,

$$\begin{aligned} \epsilon &= 1, \quad \Gamma = \mu & \text{for } \mu < 1 \\ \epsilon &= \mu, \quad \Gamma = 1/\mu & \text{for } \mu \geq 1 \end{aligned}$$

The excitation energies above the ground state can be obtained by diagonalizing the Hamiltonian  $\hat{\mathcal{H}}_2$ , which can be achieved by canonical transformation of bosonic operators [112–114],

$$\hat{b}_1^\dagger = \frac{(\omega_- + \epsilon)(\hat{a}_1^\dagger - \hat{a}_2^\dagger) + (\omega_- - \epsilon)(\hat{a}_1 - \hat{a}_2)}{2\sqrt{2}\epsilon\omega_-} \quad (\text{A6a})$$

$$\hat{b}_2^\dagger = \frac{(\omega_+ + \epsilon)(\hat{a}_1^\dagger + \hat{a}_2^\dagger) + (\omega_+ - \epsilon)(\hat{a}_1 + \hat{a}_2)}{2\sqrt{2}\epsilon\omega_+} \quad (\text{A6b})$$

where the new set of operators satisfy the commutation relation  $[\hat{b}_i, \hat{b}_j^\dagger] = \delta_{ij}$ . The diagonal form of the Hamiltonian is given by,

$$\begin{aligned} \hat{\mathcal{H}}_2 &= \sqrt{\epsilon^2 - \Gamma\epsilon} \hat{b}_1^\dagger \hat{b}_1 + \sqrt{\epsilon^2 + \Gamma\epsilon} \hat{b}_2^\dagger \hat{b}_2 + E_0 \\ &= \omega_- \hat{b}_1^\dagger \hat{b}_1 + \omega_+ \hat{b}_2^\dagger \hat{b}_2 + E_0 \end{aligned} \quad (\text{A7})$$

where  $\omega_\pm$  are the frequency of the collective modes, which matches exactly with the small amplitude oscillation frequencies (Eq.(10)) obtained from linear stability analysis. The zero point energy due to quantum fluctuation is given by  $E_0 = [\sqrt{\epsilon^2 + \Gamma\epsilon} + \sqrt{\epsilon^2 - \Gamma\epsilon} - 2\epsilon]/2$ .

Vanishing of the energy gap leads to the enhanced quantum fluctuations at the critical point which can be observed in the spin fluctuation. Within the HP transformation, we obtain the spin fluctuation of the ground state  $\chi_{1z} = \langle \hat{S}_{1z}^2 \rangle - \langle \hat{S}_{1z} \rangle^2$  corresponding to a particular spin sector ( $S_1$ ),

$$\begin{aligned} \chi_{1z} &= \frac{S}{2} \cos^2 \theta_1 \left[ \frac{(\epsilon - \omega_-)^2}{\epsilon\omega_-} + \frac{(\epsilon - \omega_+)^2}{\epsilon\omega_+} \right] \\ &+ \frac{S}{4} \epsilon \sin^2 \theta_1 \left[ \frac{1}{\omega_-} + \frac{1}{\omega_+} \right] \end{aligned} \quad (\text{A8})$$

which diverges at the critical coupling strength  $\mu_c$ , as shown in Fig.A1.

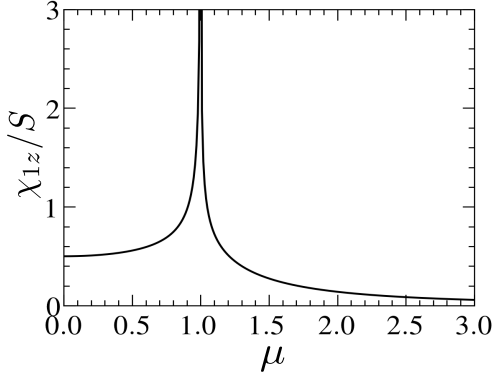


FIG. A1: Signature of QPT from the singular behavior of spin fluctuation  $\chi_{1z}/S$  at the critical coupling strength  $\mu_c$ .

### Appendix B: Effective potential of the Coupled top model

Similar to the Landau free energy for continuous phase transition, the coupled top model can equivalently be described by an effective potential, which elucidates the quantum phase transition, and its connection with ES-QPT. Following the prescription of HP transformation, we define the canonically conjugate variables  $Q_i, P_i$  in terms of the bosonic creation  $a_i^\dagger$  and annihilation  $a_i$  operators as,

$$Q_i = \frac{a_i^\dagger + a_i}{\sqrt{S}}, \quad P_i = i \frac{a_i^\dagger - a_i}{\sqrt{S}} \quad (\text{B1})$$

which can be treated classically in the limit  $S \rightarrow \infty$ . Using the HP transformation, the spin components can be written in terms of these variables as,

$$\tilde{S}_{ix} = \frac{S}{\sqrt{2}} Q_i \sqrt{1 - \frac{Q_i^2 + P_i^2}{8}} \quad (\text{B2a})$$

$$\tilde{S}_{iy} = \frac{S}{\sqrt{2}} P_i \sqrt{1 - \frac{Q_i^2 + P_i^2}{8}} \quad (\text{B2b})$$

$$\tilde{S}_{iz} = S \left( 1 - \frac{Q_i^2 + P_i^2}{4} \right) \quad (\text{B2c})$$

In the symmetry unbroken phase with  $\mu < \mu_c$ , spins are aligned along the  $x$ -axis in the ground state of the system. For such classical spin orientation we perform a spin rotation around the  $y$ -axis, which yields  $\tilde{S}_{ix} = S_{iz}$  and  $\tilde{S}_{iz} = -S_{ix}$  and in terms of the classical variables  $Q_i, P_i$  the corresponding classical Hamiltonian (scaled by  $S$ ) can be written as,

$$\mathcal{H}_{cl} = -2 + \frac{Q_1^2 + P_1^2}{4} + \frac{Q_2^2 + P_2^2}{4} - \frac{\mu}{2} Q_1 Q_2 \sqrt{1 - \frac{Q_1^2 + P_1^2}{8}} \sqrt{1 - \frac{Q_2^2 + P_2^2}{8}}. \quad (\text{B3})$$

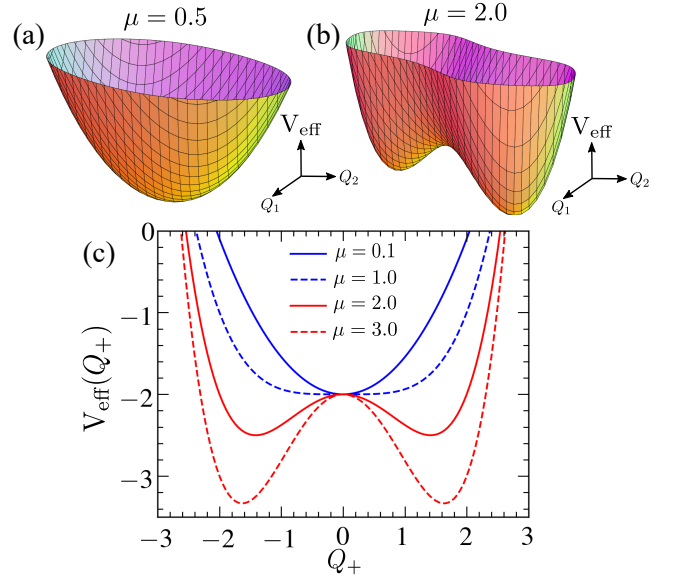


FIG. B1: Effective potential (a) before and (b) after QPT, exhibiting the symmetry breaking phenomena. (c) Cross section of effective potential with  $Q_- = 0$  for different values of  $\mu$ . Blue (red) lines denote the potential for  $\mu \leq \mu_c$  ( $\mu > \mu_c$ ).

Minimization of the energy leads to the conditions  $P_1 = P_2 = 0$  and thus we obtain the effective potential for CT model,

$$V_{\text{eff}} = -2 + \frac{Q_1^2 + Q_2^2}{4} - \frac{\mu}{2} Q_1 Q_2 \sqrt{1 - \frac{Q_1^2}{8}} \sqrt{1 - \frac{Q_2^2}{8}}. \quad (\text{B4})$$

It can be seen from Fig.B1(a), below  $\mu_c$ , the effective potential  $V_{\text{eff}}$  has a single minimum at  $Q_1 = Q_2 = 0$ , which corresponds to the symmetry unbroken steady state FP-I with energy  $E = -2$ . Whereas above the phase transition  $\mu > \mu_c$ , the potential changes its shape to double well structure (see Fig.B1(b)), which clearly captures the symmetry breaking phenomenon associated with QPT. The energy of the two minima of this potential matches with that of the symmetry broken steady state FP-III. Above the QPT with  $\mu > \mu_c$ , the point  $Q_1 = Q_2 = 0$  corresponds to the maximum of the potential barrier in  $V_{\text{eff}}$  which schematically describes the ESQPT with critical energy density  $E_c = -2$ , separating the symmetry broken states (within the double well) from the symmetry unbroken sector above the barrier. The Hamiltonian given in Eq.(B3) remains invariant under the exchange of the variables ( $Q_1 \leftrightarrow Q_2, P_1 \leftrightarrow P_2$ ). Therefore, we redefine the variables as,  $Q_{\pm} = (Q_1 \pm Q_2)/2$  and the effective potential (Eq.(B4)) can be rewritten in terms of these new variables. It can be shown, the minimization of this redefined potential leads to the condition  $Q_- = 0$ , which is in accordance with the fact that, due to the ferromagnetic ordering of the ground state, the spins are aligned. Using the condition  $Q_- = 0$ , the potential can be written

in terms of  $Q_+$  as,

$$V_{\text{eff}}(Q_+) = -2 + \frac{Q_+^2}{2} - \frac{\mu}{2} \left( Q_+^2 - \frac{Q_+^4}{8} \right) \quad (\text{B5})$$

The nature of this potential as a function of  $Q_+$ , in the different coupling regime is presented in the Fig.B1(c), which capture the signature of quantum phase transition. Furthermore, It is evident from the Fig.B1(c) that, the ESQPT corresponds to the barrier between the two well, and the barrier height corresponds to the critical energy density  $E_c = -2$ .

### Appendix C: Signature of Quantum phase transition in the multifractal dimension

The change in the structure of ground state wavefunction across the quantum critical point can be captured from the sudden change in fractal dimension  $D_q$ , which signifies the occurrence of quantum phase transition. Before the transition ( $\mu < \mu_c$ ), both spins of the CT model are aligned along the  $x$ -axis, as a result, a few eigenstates of  $\hat{S}_{ix}$  operators with large eigenvalues participate in the ground state. Hence, the ground state remains localized in the basis  $|m_{1x}, m_{2x}\rangle$ , where  $m_{ix}$  is the eigenvalue of  $\hat{S}_{ix}$ . Consequently, before QPT, the multifractal dimension  $D_q$  computed in the above basis yields small value indicating localization. On the other hand, the spin orientation changes above the critical coupling  $\mu_c$  and more number of eigenstates contribute to the ground state. Such change in the structure of the ground state is reflected from rapid growth in multifractal dimension  $D_q$  across the QPT as shown in Fig.C1.

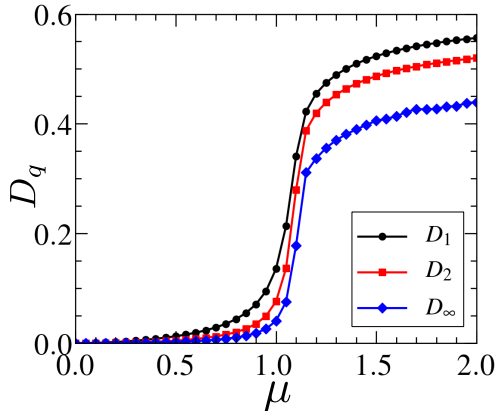


FIG. C1: Signature of QPT from the multifractal dimension  $D_q$  of the ground state as a function of  $\mu$ .

### Appendix D: Integrability at large coupling strength

The coupled top model becomes integrable at two extreme limits of coupling strength  $\mu$ . In the presence of

weak interaction ( $\mu \rightarrow 0$ ), two spins precess independently around the  $x$ -axis and the system becomes integrable. At the quantum level, this is manifested by Poissonian level spacing distribution in the small coupling regime  $\mu < \mu_c$ . Moreover, in the opposite limit ( $\mu \gg 1$ ) where the interaction between the two spins becomes large compared to the precession term, the model is nearly integrable. To study the system in this extreme limit, we scale the Hamiltonian (given in Eq.(1)) by  $\mu$ , which can be written as,

$$\hat{\mathcal{H}} = -\epsilon(\hat{S}_{1x} + \hat{S}_{2x}) - \frac{1}{S} \hat{S}_{1z} \hat{S}_{2z} \quad (\text{D1})$$

where  $\epsilon = 1/\mu$  and  $\epsilon \rightarrow 0$  for  $\mu \rightarrow \infty$ . The above Hamiltonian can be written classically in terms of the collective coordinates as,

$$\mathcal{H}_{cl} = -\epsilon \left[ \sqrt{1 - z_1^2} \cos \phi_1 + \sqrt{1 - z_2^2} \cos \phi_2 \right] - z_1 z_2. \quad (\text{D2})$$

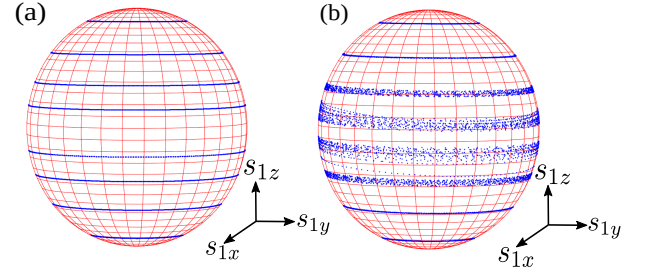


FIG. D1: Comparison of phase space trajectories on Bloch sphere corresponding to a particular spin sector for (a)  $\epsilon = 0$  and (b)  $\epsilon = 0.01$ , exhibiting diffusive behavior of the trajectories near the equator with  $E \approx 0$ , as a result of deviation from ergodicity for  $\epsilon > 0$ .

For  $\epsilon = 0$ , the classical Hamiltonian  $\mathcal{H}_{cl}$  given in Eq.(D2) is independent of the angle variables  $\phi_i$ , and the EOM yields the solution  $\phi_i = z_i t + c$  with constant  $z_i$ , which represents precession of spins around the  $z$ -axis as depicted in Fig.D1(a). As  $\epsilon$  increases, the dynamics near the equator of the Bloch sphere corresponding to the energy  $E \approx 0$  becomes diffusive, whereas regular trajectories are observed near the poles (see Fig.D1(b)). The above results obtained from classical analysis at large  $\mu$  are also supported by quantum analysis as well. To see this, we sort the energy levels obtained from exact diagonalization of the above Hamiltonian (Eq.(D1)) in ascending order, belonging to a particular parity as well as exchange symmetry sector (mentioned in main text). Next, we compute the level spacing  $\delta_\nu = \mathcal{E}_\nu - \mathcal{E}_{\nu-1}$  which is shown with increasing value of the index  $\nu$  in Fig.D2(a). For the integrable limit with  $\epsilon = 0$ , the level spacings are distributed in a regular fashion compared to the that for  $\epsilon \neq 0$ . However, for  $\epsilon \ll 1$ , the level spacings corresponding to very low as well as high energy states show almost regular structure, whereas those at the middle of

the spectrum ( $E \approx 0$ ) exhibits significant deviation which is consistent with the classical picture (see Fig.D2(a)). Also, such deviation increases as the Hamiltonian differs from the integrable limit with increasing value of  $\epsilon$ . A similar analysis has also been done in the context of Dicke model [114].

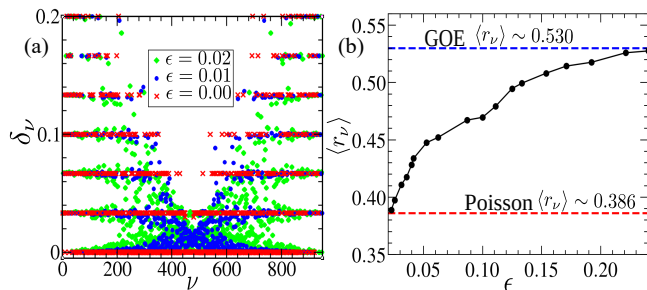


FIG. D2: (a) Level spacing  $\delta_\nu$  with increasing index  $\nu$  of ordered eigenvalues (of even symmetry sector), for different values of  $\epsilon$ . The eigenstates near both edges of the energy band exhibit regular spacing  $\delta_\nu$ , as the integrable limit is approached with decreasing  $\epsilon$ . (b) Variation of average ratio of consecutive level spacing  $\langle r_\nu \rangle$  with  $\epsilon$ , exhibiting crossover from GOE to Poisson statistics. Red (blue) dashed lines denote the Poisson (GOE) limit of  $\langle r_\nu \rangle$ .

- 
- [1] S. Sachdev, *Quantum Phase Transitions* (Cambridge University Press, Cambridge, 1999).
- [2] L. Amico, R. Fazio, A. Osterloh, and V. Vedral, *Rev. Mod. Phys.* **80**, 517 (2008).
- [3] L. D'Alessio, Y. Kafri, A. Polkovnikov, and M. Rigol, *Adv. Phys.* **65**, 239 (2016).
- [4] A. Polkovnikov, K. Sengupta, A. Silva, and M. Vengalattore, *Rev. Mod. Phys.* **83**, 863 (2011).
- [5] J. Eisert, M. Friesdorf, and C. Gogolin, *Nat. Phys.* **11**, 124 (2015).
- [6] P. Cejnar, P. Stránský, M. Macek, and M. Kloc, *J. Phys. A* **54** (2021) 133001.
- [7] P. Cejnar, M. Macek, S. Heinze, J. Jolie, and J. Dobeš, *J. Phys. A* **39**, L515 (2006).
- [8] M. A. Caprio, P. Cejnar, and F. Iachello, *Ann. Phys. (NY)* **323**, 1106 (2008); P. Cejnar and P. Stránský, *Phys. Rev. E* **78**, 031130 (2008).
- [9] P. Stránský, M. Macek, and P. Cejnar, *Ann. Phys. (NY)* **345**, 73 (2014); P. Stránský, M. Macek, A. Leviathan, and P. Cejnar, *ibid.* **356**, 57 (2015).
- [10] T. Brandes, *Phys. Rev. E* **88**, 032133 (2013).
- [11] P. Pérez-Fernández and A. Relaño, *Phys. Rev. E* **96**, 012121 (2017).
- [12] L. F. Santos, M. Távora, and F. Pérez-Bernal, *Phys. Rev. A* **94**, 012113 (2016); L. F. Santos and F. Pérez-Bernal, *ibid.* **92**, 050101(R) (2015); P. Riberio, J. Vidal, and R. Mosseri, *Phys. Rev. E* **78**, 021106 (2008).
- [13] R. Vasseur and J. E. Moore, *J. Stat. Mech.* (2016) 064010.
- [14] E. Altman, Non equilibrium quantum dynamics in ultra-cold quantum gases, in *Strongly Interacting Quantum Systems out of Equilibrium*, edited by T. Giamarchi, A. J. Millis, O. Parcollet, H. Saleur, and L. F. Cugliandolo, Lecture Notes of the Les Houches Summer School Vol. 99 (Oxford University Press, Oxford, 2016).
- [15] T. Langen, R. Geiger, and J. Schmiedmayer, *Annu. Rev. Condens. Matter Phys.* **6**, 201 (2015).
- [16] M. Rigol, V. Dunjko, and M. Olshanii, *Nature (London)* **452**, 854 (2008); M. Rigol, V. Dunjko, V. Yurovsky, and M. Olshanii, *Phys. Rev. Lett.* **98**, 050405 (2007).
- [17] L. Vidmar and M. Rigol, *J. Stat. Mech.* (2016) 064007.
- [18] T. Langen et al., *Science* **348**, 207 (2015).
- [19] M. Gring et al., *Science* **337**, 1318 (2012).
- [20] J.-S. Caux, R. M. Konik, *Phys. Rev. Lett.* **109**, 175301 (2012).
- [21] S. Maity, U. Bhattacharya, A. Dutta, and D. Sen, *Phys. Rev. B* **99**, 020306(R) (2019).
- [22] J. M. Deutsch, *Phys. Rev. A* **43**, 2046 (1991).
- [23] M. Srednicki, *Phys. Rev. E* **50**, 2 (1994).
- [24] F. M. Izrailev, *Phys. Rep.* **196**, 299 (1990).
- [25] F. Borgonovi, F. M. Izrailev, L. F. Santos, and V. G. Zelevinsky, *Phys. Rep.* **626**, 1 (2016).
- [26] R. Nandkishore and D. A. Huse, *Annu. Rev. Condens. Matter Phys.* **6**, 15 (2015).
- [27] D. A. Abanin and Z. Papić, *Ann. Phys. (Berlin)* **529**, 1700169 (2017).
- [28] E. Altman, *Nat. Phys.* **14**, 979 (2018); D. A. Abanin, E. Altman, I. Bloch, M. Serbyn, *Rev. Mod. Phys.* **91**, 021001 (2019).
- [29] B. L. Altshuler, E. Cuevas, L. B. Ioffe, and V. E. Kravtsov, *Phys. Rev. Lett.* **117**, 156601 (2016).
- [30] X. Deng, S. Ray, S. Sinha, G. V. Shlyapnikov, and L. Santos, *Phys. Rev. Lett.* **123**, 025301 (2019).
- [31] A. Russomanno, M. Fava, and R. Fazio, *Phys. Rev. B*

- 102**, 144302 (2020).
- [32] D. J. Luitz and Y. B. Lev, Phys. Rev. Lett. **117**, 170404 (2016).
- [33] P. Bordia, H. Lschen, U. Schneider, M. Knap, and I. Bloch, Nat. Phys. **13**, 460 (2017); P. Bordia, H. Lschen, S. Scherg, S. Gopalakrishnan, M. Knap, U. Schneider, and I. Bloch, Phys. Rev. X **7**, 041047 (2017).
- [34] M. Schreiber et al., Science **349**, 842 (2015).
- [35] L. D'Alessio and A. Polkovnikov, Ann. Phys. **333**, 19-33 (2013).
- [36] M. Serbyn, Z. Papić, and D. A. Abanin, Phys. Rev. X **5**, 041047 (2015).
- [37] A. Lazarides, A. Das, and R. Moessner Phys. Rev. Lett. **115**, 030402 (2015); E. Bairey, G. Refael, and N. H. Lindner, Phys. Rev. B **96**, 020201(R) (2017).
- [38] B. L. Altshuler and G. V. Shlyapnikov, Phys. Rev. Lett. **113**, 045304 (2014).
- [39] S. Ray, A. Ghosh, and S. Sinha, Phys. Rev. E **97**, 010101(R) (2018); S. Ray, B. Mukherjee, S. Sinha, and K. Sengupta, Phys. Rev. A **96**, 023607 (2017).
- [40] P. W. Claeys and A. Lamacraft, Phys. Rev. Lett. **126**, 100603 (2021).
- [41] K. Klobas, B. Bertini, and L. Piroli, Phys. Rev. Lett. **126**, 160602 (2021).
- [42] H. Bernien, S. Schwartz, A. Keesling et al., Nature (London) **551**, 579 (2017).
- [43] C. J. Turner, A. A. Michailidis, D. A. Abanin, M. Serbyn, and Z. Papić, Nat. Phys. **14**, 745 (2018).
- [44] C. J. Lin and O. I. Motrunich, Phys. Rev. Lett. **122**, 173401 (2019).
- [45] S. Choi et. al., Phys. Rev. Lett. **122**, 220603 (2019).
- [46] W. W. Ho, S. Choi, H. Pichler, and M. D. Lukin, Phys. Rev. Lett. **122**, 040603 (2019).
- [47] A. A. Michailidis, C. J. Turner, Z. Papić, D. A. Abanin, and M. Serbyn, Phys. Rev. X **10**, 011055 (2020).
- [48] M. Schecter and T. Iadecola, Phys. Rev. Lett. **123**, 147201 (2019).
- [49] N. Shibata, N. Yoshioka, and H. Katsura, Phys. Rev. Lett. **124**, 180604 (2020).
- [50] A. Hudomal, I. Vasić, N. Regnault, and Z. Papić, Commun. Phys. **3**, 99 (2020).
- [51] S. Pai and M. Pretko, Phys. Rev. Lett. **123**, 136401 (2019).
- [52] H. Zhao, J. Vovrosh, F. Mintert, and J. Knolle, Phys. Rev. Lett. **124**, 160604 (2020).
- [53] S. Sugiura, T. Kuwahara, and K. Saito, Phys. Rev. Research **3**, L012010 (2021).
- [54] S. Chattopadhyay, H. Pichler, M. D. Lukin, and W. W. Ho, Phys. Rev. B **101**, 174308 (2020).
- [55] B. Mukherjee, S. Nandy, A. Sen, D. Sen, and K. Sengupta, Phys. Rev. B **101**, 245107 (2020).
- [56] N. Shiraishi, J. Stat. Mech. (2019) 083103.
- [57] D. K. Mark, C. J. Lin, and O. I. Motrunich, Phys. Rev. B **101**, 195131 (2020).
- [58] S. Sinha and S. Sinha, Phys. Rev. Lett. **125**, 134101 (2020).
- [59] D. Mondal, S. Sinha, and S. Sinha, Phys. Rev. E **102**, 020101(R) (2020).
- [60] E. Heller, Phys. Rev. Lett. **53**, 1515 (1984).
- [61] A. Altland and F. Haake, Phys. Rev. Lett. **108**, 073601 (2012); New J. Phys **14**, 73011 (2012).
- [62] S. Ray, A. Ghosh, and S. Sinha, Phys. Rev. E **94**, 032103 (2016).
- [63] D. Mondal, S. Sinha, and S. Sinha, [arXiv:2104.15093](https://arxiv.org/abs/2104.15093).
- [64] S. H. Shenker and D. Stanford, J. High Energy Phys. **05** (2015) 132; S. H. Shenker and D. Stanford, J. High Energy Phys. **03** (2014) 067.
- [65] J. Maldacena, S. H. Shenker, and D. Stanford, J. High Energy Phys. **08** (2016) 106.
- [66] K. Hashimoto, K. Murata, and R. Yoshii, J. High Energy Phys. **10** (2017) 138.
- [67] E. B. Rozenbaum, S. Ganeshan, and V. Galitski, Phys. Rev. Lett. **118**, 086801 (2017).
- [68] M. Gärttner, P. Hauke, and A. M. Rey, Phys. Rev. Lett. **120**, 040402 (2018).
- [69] A. A. Patel, D. Chowdhury, S. Sachdev, and B. Swingle, Phys. Rev. X **7**, 031047 (2017).
- [70] B. Swingle, G. Bentsen, M. Schleier-Smith, and P. Hayden, Phys. Rev. A **94**, 040302(R) (2016); P. Hosur, X. L. Qi, D. A. Roberts, and B. Yoshida, J. High Energy Phys. **02** (2016) 004.
- [71] J. Li, R. Fan, H. Wang, B. Ye, B. Zeng, H. Zhai, X. Peng, and J. Du, Phys. Rev. X **7**, 031011 (2017).
- [72] M. Gärttner, J. Bohnet, A. Safavi-Naini, M. Wall, J. Bollinger, and A. M. Rey, Nat. Phys. **13**, 781 (2017).
- [73] S. Pappalardi, A. Russomanno, B. Žunković, F. Iemini, A. Silva, and R. Fazio, Phys. Rev. B **98**, 134303 (2018).
- [74] R. J. Lewis-Swan, A. Safavi-Naini, J. J. Bollinger, and A. M. Rey, Nat. Commun. **10**, 1581 (2019).
- [75] S. Cameo, J. Carlos, M. Magnani, P. Stránský, S. Hernández, L. Santos, and J. Hirsch, Phys. Rev. E **101**, 010202(R) (2020).
- [76] I. García-Mata, M. Saraceno, R. A. Jalabert, A. J. Roncaglia, and D. A. Wisniacki, Phys. Rev. Lett. **121**, 210601 (2018).
- [77] R. Prakash and A. Lakshminarayan, Phys. Rev. B **101**, 121108 (2020).
- [78] S. Ray, S. Sinha, and K. Sengupta, Phys. Rev. A **98**, 053631 (2018).
- [79] S. Sinha, S. Ray, and S. Sinha, J. Phys.: Condens. Matter **33**, 174005 (2021).
- [80] D. T. Robb and L.E Reichl, Phys. Rev. E **57**, 2458 (1998).
- [81] J. Emerson and L.E. Ballentine, Phys. Rev. A **63**, 052103 (2001).
- [82] B. Skellett and C. A. Holmes, InterJournal Complex Syst. **518**, (2002).
- [83] A. P. Hines, R. H. McKenzie and G. J. Milburn, Phys. Rev. A **71**, 042303 (2005).
- [84] S. Ray, S. Sinha, and D. Sen, Phys. Rev. E **100**, 052129 (2019).
- [85] P. Pfeuty, Ann. Phys. (Paris) **57**, 79 (1970); P. Pfeuty and R.J. Elliott, J. Phys. C **4**, 2370 (1971).
- [86] T. Zibold, E. Nicklas, C. Gross, and M. K. Oberthaler, Phys. Rev. Lett. **105**, 204101 (2010).
- [87] A. Smerzi, S. Fantoni, S. Giovanazzi, and S. R. Shenoy, Phys. Rev. Lett. **79**, 4950 (1997); S. Raghavan, A. Smerzi, S. Fantoni, and S. R. Shenoy, Phys. Rev. A **59**, 620 (1999).
- [88] T. Holstein and H. Primakoff, Phys. Rev. **58**, 1098 (1949).
- [89] S. H. Strogatz, *Nonlinear Dynamics and Chaos*, 2007 (Westview Press, Boulder, 2007).
- [90] A. J. Lichtenberg and M. A. Leiberman, *Regular and chaotic dynamics*, (Springer-Verlag,1992).
- [91] J. Chávez-Carlos, M. A. Bastarrachea-Magnani, S. Lerma-Hernández, and J. G. Hirsch Phys. Rev. E **94**,

- 022209 (2016).
- [92] M. V. Berry and M. Tabor, Proc. R. Soc. A **356**, 375 (1977).
- [93] O. Bohigas, M. J. Giannoni, and C. Schmit, Phys. Rev. Lett. **52**, 1 (1984).
- [94] F. Haake, *Quantum Signatures of Chaos*, Springer Science and Business Media (Springer, Berlin, Heidelberg, 2013), Vol. **54**.
- [95] M. L. Mehta, *Random Matrices*, 3rd ed. (Elsevier, Amsterdam, 2004), Vol. **142**.
- [96] Y. Y. Atas, E. Bogomolny, O. Giraud, and G. Roux, Phys. Rev. Lett. **110**, 084101 (2013); V. Oganessian and D. A. Huse, Phys. Rev. B **75**, 155111 (2007).
- [97] D. N. Page, Phys. Rev. Lett. **71**, 1291 (1993).
- [98] Y. Y. Atas and E. Bogomolny, Phys. Rev. E **86**, 021104 (2012); Philos. Trans. R. Soc. Lond. A **372**, 20120520 (2014).
- [99] E. J. Torres-Herrera and L. F. Santos, Ann. Phys. (Berlin) **527**, 1600284 (2017).
- [100] J. Lindinger, A. Buchleitner, and A. Rodríguez, Phys. Rev. Lett. **122**, 106603 (2019).
- [101] A. Becker, M. Haque, and I. M. Khaymovich, Phys. Rev. E **100**, 03211 (2019).
- [102] G. D. Tomasi, and I. M. Khaymovich, Phys. Rev. Lett. **124**, 200602 (2020).
- [103] J. M. Radcliffe, J. Phys. A **4**, 313 (1971).
- [104] A. Piga, M. Lewenstein, and J. Q. Quach, Phys. Rev. E **99**, 032213 (2019).
- [105] S. Ghose, R. Stock, P. Jessen, R. Lal, and A. Silberfarb, Phys. Rev. A **78**, 042318 (2008); X. Wang, S. Ghose, B. C. Sanders, and B. Hu, Phys. Rev. E **70**, 016217 (2004).
- [106] C. Neil et. al., Nat. Phys. **12**, 1037 (2016).
- [107] E. J. Torres-Herrera and L. F. Santos, Phys. Rev. A **90**, 033623 (2014); E. J. Torres-Herrera, M. Vyas, and L. F. Santos, New J. Phys. **16**, 063010 (2014).
- [108] A. I. Larkin and Y. N. Ovchinnikov, Zh. Eksp. Teor. Fiz. **55**, 2262 (1968); [Sov. Phys. JETP **28**, 1200 (1969)].
- [109] M. V. Berry, J. Phys. A: Math. Gen. **10**, 2083 (1977).
- [110] H. Lipkin, N. Meshkov, and A. Glick, Nuclear Physics **62**, 188 (1965); N. Meshkov, A. J. Glick, and H. J. Lipkin, *ibid.* **62**, 199 (1965); A. J. Glick, H. J. Lipkin, and N. Meshkov, *ibid.* **62**, 211 (1965).
- [111] I.S. Gradshteyn and I.M. Ryzhik, *Table of Integrals, Series, and Products*, 8th Edition, D. Zwillinger, ed. (Academic Press, 2014).
- [112] V. Hakim and V. Ambegaokar, Phys. Rev. A **32**, 423 (1985).
- [113] D. Tolkunov and D. Solenov, Phys. Rev. B **75**, 024402 (2007).
- [114] C. Emary and T. Brandes, Phys. Rev. E **67**, 066203 (2003).